Plasmons in a layered strange metal using the gauge/gravity duality

Utrecht University

Master's Thesis: Theoretical Physics

Author:
Sigert Van den Eede

Supervisor:
Prof. dr. ir. H.T.C. (Henk) Stoof

February 2024

Abstract

In an attempt to understand the density-density response of the cuprate superconductors, we study plasmons in a layered strange metal using the Gubser-Rocha model. The latter is a well-known bottom-up holographic model for a strange metal that is used here to describe the strongly repulsive on-site interactions between the electrons in each copper-oxide (CuO_2) layer, whereas the long-range Coulomb interactions are incorporated by a so-called double-trace deformation. To be able to model the bilayer cuprates more realistically, we consider in particular the case of two closely-spaced CuO_2 layers per unit cell. In the response we then obtain for vanishing out-of-plane momentum both an optical and an acoustic plasmon, whereas for nonvanishing out-of-plane momentum there are two acoustic plasmon modes. We present the full density-density spectral functions with parameters typical for cuprates and discuss both the dispersion and the lifetime of these plasmon excitations. We also compute the conductivity after introducing disorder into the system and introduce the loss function to facilitate a comparison with experimental results. Finally, we also treat the effects of Umklapp scattering and inter-layer hopping on the density-density response.

Contents

Introduction

For decades condensed-matter physicists have found themselves scratching their heads over strange metals, grappling with its defining properties that completely go against predictions from Fermi-liquid theory. A standout feature, and perhaps the most perplexing one, is the perfect linear relationship between resistivity and temperature in these materials [1–3], while in a Fermi liquid the resistivity scales with temperature squared. Furthermore, the linear behavior exceeds the Mott-Ioffe-Regel limit [4], which stipulates that the resistivity becomes constant at a certain temperature, and even persists up to the material's melting point. These strange properties are presumed to be linked to the unusually strong interactions between charge carriers inside the strange metal [5,6]. But so far a comprehensive explanation for all these properties remains unknown.

Strange metals were discovered as the metallic phase of certain high-temperature superconductors called cuprates, which have a common structure of copper-oxide (CuO_2) planes. In the 1980s they sent a shock through the physics community due to their incredibly high critical temperature (T_c). Prior to the discovery of these high-temperature superconductors it was believed that superconductivity might reach a dead end. Due to the fact that the conventional superconductivity theory of Bardeen, Cooper and Schrieffer (BCS) [7] predicts a maximum critical temperature of approximately 40 Kelvin [8]. Subsequently, this maximum was spectacularly violated by the cuprate superconductors, see Fig. 1.1. After the first cuprate, many more were discovered and a critical temperature of around 135 Kelvin was reached [9]. A satisfying explanation for this relatively high temperature is still missing. For conventional superconductivity the normal metallic phase was first described by Fermi-liquid theory, on which the workings of superconductivity was then based. Therefore, it seems logical that we first need to properly grasp the strange metal in order to understand the cuprate superconductors and perhaps increase the critical temperature in the future. Achieving room-temperature superconductivity at atmospheric pressure is one of the greatest goals of condensed-matter physics.

In this thesis, we use a holographic model to investigate the properties of charge-density oscillations, better known as plasmons, in the strange-metal phase of cuprate superconductors. The plasmons in this class of materials have been studied in several experiments before [11–19]. Our goal is to attempt to gain more insight into these experiments, in particular by including one of the defining characteristics of strange metals, the linear-in-T resistivity. It is usually assumed that an understanding of these experiments requires a theory which models the effects of the strong on-site Coulomb (Hubbard-U) repulsion between the electrons in the strange-metal phase. One way to achieve this is to apply a technique that originates from string theory, known as the gauge/gravity duality or
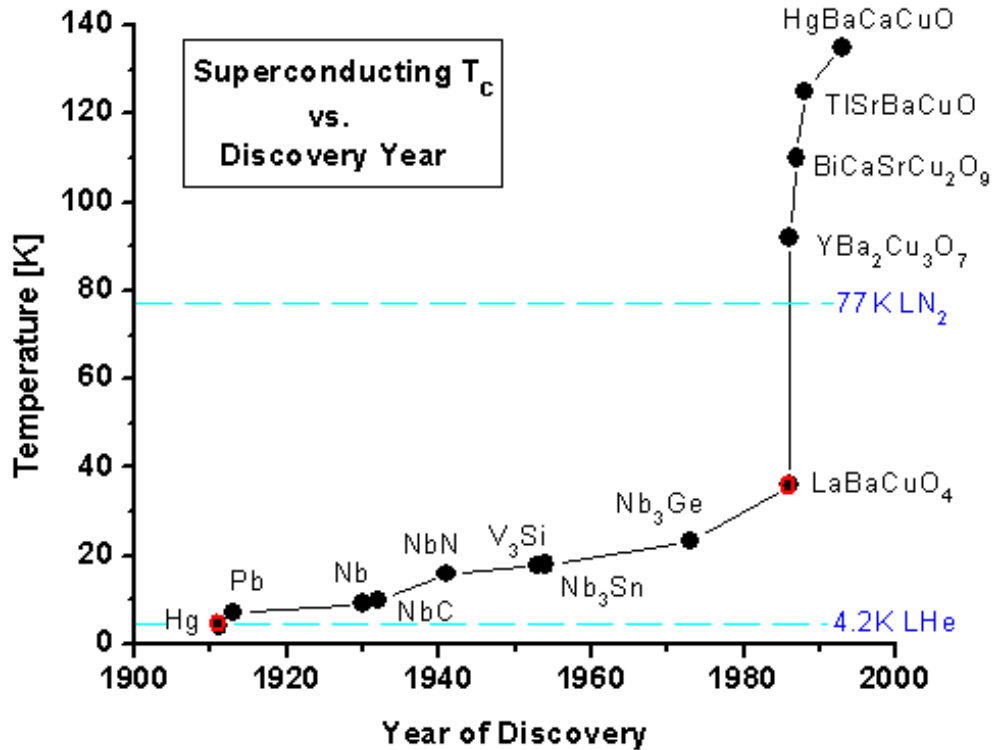
Figure 1.1: History of critical temperature of superconductors. The material YBa$_2$Cu$_3$O$_7$ is the first to surpass the liquid nitrogen temperature of 77 Kelvin. The red dots indicate Nobel prizes awarded to the discoverers. Source: [10].

AdS/CFT correspondence [20]. This correspondence conjectures that there is a relationship between a bulk gravity theory in an anti-de Sitter (AdS) spacetime and a conformal field theory (CFT) on its boundary. Since this is a bulk-boundary correspondence it is also known as the holographic principle, which has proven in recent years to effectively describe low-energy properties of strongly interacting systems [21]. This duality allows us to map the quantum field theory of the CuO$_2$ layers to a more tractable problem on the gravity side. Since the birth of this correspondence a vast amount of theories have been proposed, from these we will use the Gubser-Rocha model [22], which is a special case of an Einstein-Maxwell-dilaton model. In this model the entropy scales linearly with temperature, and hence the resistivity is also linear in temperature, which is one of the defining features of a strange metal. Moreover, recent Angle-Resolved Photo-Emission Spectroscopy (ARPES) experiments have been accurately described by the Gubser-Rocha model [23].

Ultimately, and most importantly for our purposes, this model gives us a long-wavelength density-density response function for a single CuO$_2$ layer. In principle this can only be obtained numerically, but we will use a very accurate hydrodynamic approximation instead. The Gubser-Rocha response function describes strongly interacting but 'neutral' electrons, implying that it describes the strong on-site interactions inside each layer, but not yet the long-range effects of the Coulomb interactions which are crucial for the existence of plasmons and thus need to be incorporated separately. To incorporate these long-range interactions in the framework of the gauge/gravity duality, we need to perform a so-called double-trace deformation of the conformal field theory [24, 25]. Our objective is to determine, using this same double-trace deformation, whether the Gubser-Rocha model for a strange metal leads to an improved understanding and interpretation of experimental results.

Since our approach consists of a bottom-up holographic computation, we need to realize that response functions are only determined up to an overall constant. This is due to the Newton's constant G in the gravity theory, which is not determined from our condensed-matter system. We remedy this issue by noting that the density-density response function of the layered strange metal ultimately contains a plasma frequency, which we use to fix this single undetermined constant such that the holographically obtained plasma frequency matches exactly the experimentally measured plasma frequency. Throughout this thesis, we show how this can be achieved very explicitly, after which we present our final results in the form of the density-density spectral function that depends solely on material parameters that can in principle be determined experimentally. The spectral function will most clearly display the plasmon modes of the charge-density fluctuations, with a sharp peak denoting a long-lived collective mode since the width of the peak determines its lifetime. Moreover, it is directly related to the energy-loss function, which has been observed experimentally.

Although our approach proves to be highly general and predominantly analytical, for the sake of concreteness, we focus on the cuprate $Bi_2Sr_2CaCu_2O_{8+x}$ (Bi-2212), in the category of bismuth-based cuprates. Fig. 1.2 presents a schematic illustration of the unit cell, revealing that the crystal structure of this specific cuprate is somewhat complicated. Specifically, it features pairs of closely-spaced CuO_2 planes, with these pairs further separated by a larger distance. Notably, the unit cell encompasses four CuO_2 planes, instead of two, as adjacent pairs of CuO_2 planes are rotated by 45 degrees relative to each other. Since we are mainly interested in the long-wavelength physics we do
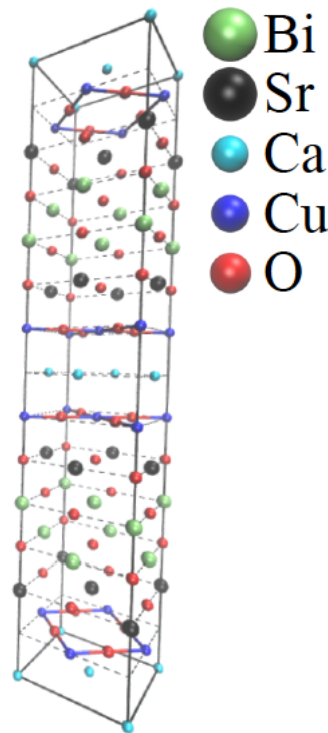
Figure 1.2: The unit cell of Bi-2212, consisting of CuO_2 planes separated by charge reservoirs. Adjacent pairs of CuO_2 planes are rotated by 45 degrees. Source: [26].

not consider this rotation and instead assume that each CuO_2 layer is identical.

The thesis is structured as follows. We start by introducing Fermi-liquid theory for ordinary metals

in Chapter 2. We discuss the resistivity and response function of these metals. Followed by the introduction of strange metals in Chapter 3, focusing on the aspects that violate Fermi-liquid theory. Moreover, we introduce Bi-2212 and its material parameters. Then, Chapter 4 is dedicated to explaining the gauge/gravity duality and introducing the Gubser-Rocha model. In Chapter 5 the first plasmon modes are presented in the form of a density-density spectral function, starting with the simplest possible configuration, one layer. Followed by adding another layer at distance a, resulting in a matrix structure in the response. Subsequently, the desired geometry of a bilayered crystal is reached in Chapter 6 by stacking pairs of layers on top of each other with a distance l between the pairs. The main results of the thesis are presented in this chapter. On top of computing the spectral function we also compute the conductivity after introducing Planckian dissipation. In turn this allows the computation of the loss function, making our results readily comparable to experiments. Then we shift our focus to extensions of the model, first we consider Umklapp scattering due to supermodulation and display the results in the form of spectral functions and loss functions. Thereafter, we introduce hopping between the layers by altering the holographic response function. The hopping induces a gap at zero in-plane momentum and amplifies the out-of-phase mode significantly. At the end of the chapter we reduce the bilayer-crystal response to a single-layer crystal, to verify the expression obtained with previous work in the literature. Then, Chapter 7 contains computations for other cuprates by changing the material parameters used, which allows for even more comparison with experiments.

Finally, in Chapter 8 we conclude this thesis and discuss possible future efforts to improve our understanding of strange metals.

Fermi-liquid Theory

In this chapter we shortly go over the background of condensed-matter physics, more specifically Fermi-liquid theory. Because in order to know what is strange, we first need to know what is normal.

First, we discuss how this theory came to existence, for which we have to go back to the 1950s. At the end of this period Landau developed his Fermi-liquid theory, which became the bedrock of condensed-matter physics, since it accurately describes metals in their normal state. Originally, Landau proposed the theory to describe liquid Helium (^{3}He to be exact) at low temperatures, but later it was realized that it could be used for other fermionic systems as well.

Consider the concrete example of a gas of non-interacting electrons, with the ground state of this gas given by a so-called Fermi sea of electrons, which means that the electrons fill up states up to the Fermi momentum. All energy states below are filled up and gives rise to a boundary called the Fermi surface, which separates the occupied states from the unoccupied states. Then, low-energy excitations are formed when an electron is excited from the Fermi sea, these excitations are called particle-hole excitations, since a hole is formed in the Fermi sea.

The next question to answer is: how is the Fermi liquid formed from a non-interacting Fermi gas? This is done by creating a relation between eigenstate of the non-interacting gas with those of the Fermi liquid. The interactions of the Fermi liquid are turned on adiabatically, which means infinitely slow. Landau claimed that there is a one-to-one-correspondence between these eigenstates. The particles described in Fermi liquid theory are not exactly the same as electrons anymore, but are now quasiparticles with an effective mass that can deviate from the electron mass.

2.1 Resistance of metals

The electrical resistivity of metals in the Fermi-liquid picture is not a simple formula, but depends on what interactions dominate. An important notion to introduce is the mean free path l for the electrons. This quantity indicates the average distance an electron travels before a collision occurs. The resistivity is inversely proportional to the average time between collisions, given by $\tau = l/v_F$, with v_F the Fermi velocity of the electrons. Therefore, the resistivity is inversely proportional to the temperature-dependent mean free path,

$$\rho \propto 1/l. \tag{2.1}$$

At low temperatures electron-electron scattering, giving rise to quadratic temperature dependence, and scattering off impurities in the metal are most important. The latter causing a constant temperature dependence of the resistivity. Therefore, at low temperatures the resistivity is of the following form

$$\rho \sim \rho_0 + A_{e,e} T^2, \tag{2.2}$$

where $A_{e,e}$ a parameter characterizing the resistivity caused by electron-electron scattering.
Then in a higher temperature regime electron-phonon interactions dominate. Phonons are quantized oscillations in the lattice. These interactions give rise to linear-in-T resistivity.

As it turns out the resistivity does not grow until the melting point of metals. Namely, in 1960 Ioffe and Regel reasoned that the mean free path cannot decrease indefinitely. A decrease in mean free path would arise due to the fact that electrons are more likely to scatter of phonons if the temperature increases. While the mean free path is typically much larger than the lattice spacing, it cannot become smaller than this spacing. Since then the semi-classical picture of mean free path breaks down. Due to the fact that you can expect that an electron can scatter at most at every atom. This reasoning gives us a temperature at which the resistivity saturates and becomes constant and this is called the Mott-Ioffe-Regel limit.

2.2 Random-Phase Approximation

To treat electron-electron interactions, we introduce the Random-Phase Approximation (RPA), a well-known framework by which collective behavior of particles can be described. In the high-density limit the theory even becomes exact. Central to RPA is the definition of the density-density response function, denoted as $\chi^{RPA}(\boldsymbol{q}, \omega)$. This function captures the system's response to density perturbations characterized by momentum $\boldsymbol{q}$ and frequency ω, defined as

$$\chi^{RPA}(\boldsymbol{q}, \omega) = \frac{\chi_0(\boldsymbol{q}, \omega)}{1 - V(\boldsymbol{q}) \chi_0(\boldsymbol{q}, \omega)}, \tag{2.3}$$

where $\chi_0(\boldsymbol{q}, \omega)$ represents the non-interacting (bare) density-density response function and $V(\boldsymbol{q})$ is the effective interaction potential. If desired, a more elaborate exploration of the Random-Phase Approximation and its applications is found in "Quantum Theory of the Electron Liquid" [27]. Another recommended book is "Ultracold Quantum Fields" [28].

An important implication of RPA is the fact that at long wavelengths the density-density response is dominated by a collective excitation known as the plasmon [28]. These quasiparticles arise due to long-range Coulomb interactions among electrons. The potential in the response function computed in RPA becomes the Fourier transform of the Coulomb potential

$$\begin{cases} V(\boldsymbol{q}) = \frac{e^2}{2\epsilon_0 |\boldsymbol{q}|}, & \text{2D} \\ V(\boldsymbol{q}) = \frac{e^2}{\epsilon_0 q^2}, & \text{3D}, \end{cases} \tag{2.4}$$

where 2D means that the system at hand is two-dimensional, but the Coulomb interactions still live in three dimensions. Here, ϵ_0 is the background dielectric constant and e is the electron charge. Since in the condensed-matter systems of interest the Fermi velocity is much smaller than the speed of light, the Coulomb potential is only dependent on momentum. The non-interacting density-density response function is given by

$$\chi_0(\boldsymbol{q}, \omega) = \frac{n_e}{m} \frac{q^2}{\omega^2}, \tag{2.5}$$

with n_e the density of electrons and m the electron mass. Using this equation and Eq. (2.4) the dispersion of a two-dimensional plasmon is derived by setting the denominator of Eq. (2.3) to zero. Thus we obtain

$$\omega(\boldsymbol{q}) = \sqrt{\frac{e^2 n_e}{2m\epsilon_0} |\boldsymbol{q}|}. \tag{2.6}$$

In three dimensions the Coulomb potential is inversely proportional to $\boldsymbol{q}^2$, which means that the obtained plasmon mode is gapped. Therefore, in the limit $q \to 0$ there is a plasma frequency

$$\omega_{pl} = \sqrt{\frac{e^2 n_e}{m\epsilon_0}}. \tag{2.7}$$

Strange Metals

Having introduced Fermi-liquid theory, we now move on to a non-Fermi liquid: the strange metal. This phase of matter is not described by Fermi-liquid theory and violates its principles in many ways. The most striking property of strange metals is the linear temperature dependence of the resistivity [1–3]. Contrary to Fermi-liquid theory, which predicts a quadratic temperature dependence in the resistivity for electron-electron interactions. Additionally, the resistivity of strange metals remains linear up to the material's melting point, exceeding the Mott-Ioffe-Regel limit [4]. Another unexplained feature is the quadratic temperature dependence of the Hall angle [29–31]. The cause of these violations remain a mystery and have not been fully explained yet. All in all the strange-metal phase is incredibly *strange* and has therefore been given a fitting name. But there are actually more reasons to study the strange metal apart from its unusual features. Namely, cuprate superconductors, found to have a high critical temperature, become strange metals in their normal phase. And it is believed that understanding the strange metal is fundamental for grasping the relatively high T_c of these materials.

In this chapter we first delve into cuprate superconductors in general and then consider a specific cuprate, $Bi_2Sr_2CaCu_2O_{8+x}$, also known as Bi-2212, such that we are able to directly compare with experiments.

3.1 Cuprate superconductors

In the 1980s a breakthrough occurred in the field of condensed matter when a mysterious class of materials was found which remain superconducting up to relatively high temperatures. The highest critical temperature observed for these materials, called cuprate superconductors, is about 135 K [9]. This incredible critical temperature is partly why the interest in these materials is so great, since obtaining room-temperature superconductors is one of the greatest goals of the condensed-matter community.

In Fig. 3.1 the phase diagram of a typical hole-doped cuprate is shown. The strange-metal phase resides above the doping range with largest T_c. For our purposes the other aspects of this complicated phase diagram are not important. Here the x-axis depicts the hole doping of the cuprate, which shows how many electrons have been removed from the CuO_2 layers. Then on the y-axis the temperature is shown. We will attempt to model the strange-metal phase above the center of the superconducting dome.
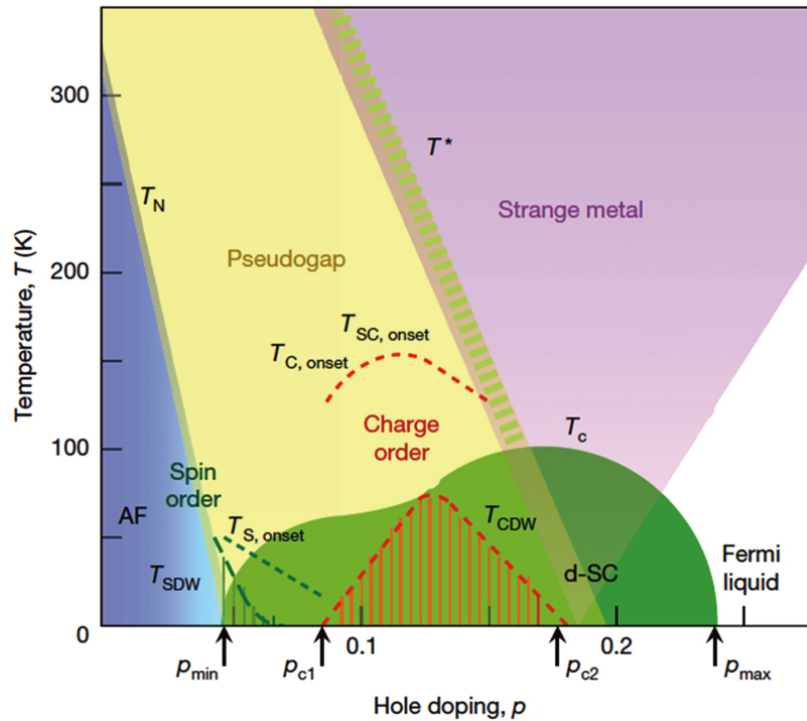
Figure 3.1: A phase diagram of hole-doped cuprates as a function of temperature and doping. The strange-metal phase is centered around a doping of approximately 0.19. Source: [32].
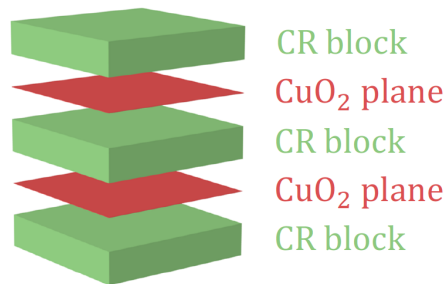
Figure 3.2: Generic structure of cuprates, the CuO_2 planes are separated by charge reservoirs. Source: [26].

The defining feature of cuprates is the stacking of CuO_2 layers, as seen in Fig. 3.2, composed of a square lattice of copper and oxygen atoms. In these layers the interactions between charge carriers are unusually strong and it is believed that these interactions cause the peculiar properties. In between these layers are charge reservoirs, whose atomic structure is much more complicated than the CuO_2 layers. Note that the resistivity along the axis perpendicular to the layers is 100 - 10^5 times larger than the in-plane resistivity [33]. Although the charge reservoirs serve as insulating layers there is coupling between the CuO_2 planes due to the Coulomb force.
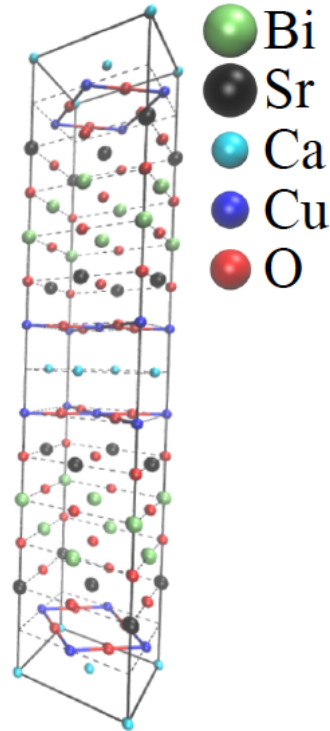
Figure 3.3: The unit cell of Bi-2212, consisting of CuO_2 planes separated by charge reservoirs. Adjacent pairs of CuO_2 planes are rotated by 45 degrees. Source: [26].

3.2 $Bi_2Sr_2CaCu_2O_{8+x}$ (Bi-2212)

In this section we discuss some of the specifics of the cuprate that we have chosen to model, Bi-2212. The unit cell is displayed in Fig. 3.3. The main aspect of interest is the bilayered structure, which means that we have pairs of closely-spaced CuO_2 planes stacked on top of each other. The distance between the closely-spaced layers is 3.2 Å (where an angstrom is equivalent to 0.1 nm) and the distance between the pairs of layers is 15.4 Å. The unit cell consists of four unit cells because adjacent CuO_2 planes are rotated by 45 degrees. We ignore this rotation because it does not affect the long-wavelength physics on the scale of many unit cells. We consider all CuO_2 layers to be the same, thus the unit cell we analyze is comprised of only two CuO_2 layers.
Moving on to specific CuO_2 layer properties, the electron density n is approximately $(0.25 \text{ Å}^{-1})^2$, which is computed by dividing the 0.85 electrons per Cu site by its surface, $(3.8 \text{ Å})^2$. The 0.85 electrons per Cu site is due to the assumption of hole doping of 0.15. Then the Fermi velocity is $v_F = 1.5\text{eV Å}/\hbar \approx 2.28 \times 10^5 \text{ ms}^{-1}$. Additionally, there is the background dielectric constant of the surrounding layers, $\epsilon/e^2 = 4.5 \times 55.263 \times 10^{-4}\text{eV}^{-1}\text{Å}^{-1}$. Lastly, the most important parameter , since it enables the use of the holographic response function is the plasma frequency, $\hbar\omega_{pl} = 1.0$ eV.

Gauge/gravity Duality

We approach the challenge of describing the strong interactions among charge carriers in the CuO_2 layers by using the gauge/gravity duality. This chapter serves as an introduction to this duality and also gives us the density-density response function that incorporates the strong interactions. We obtain this response function from the Gubser-Rocha model, which turns out to be well-suited to model the strange metal.

4.1 Introduction to holography

As mentioned before, it seems that the strong Coulomb interactions in the CuO_2 layers between charge carriers cause the strange behavior of the cuprates. Therefore, it follows that we need a clear description of these strong interactions to shed light on the workings of the strange-metallic phase. At this point the holographic principle [20], also known as either gauge/gravity duality or AdS/CFT correspondence, comes into the picture, since strongly correlated systems arise naturally in this framework.

Hence, we go back in time to explore how this duality and its applications formed. The inception of the gauge/gravity duality can be attributed to the insights of Juan Maldacena in the end of the 1990s [20]. Maldacena's remarkable discovery presented a novel perspective, conjecturing that a gravitational theory in Anti-de Sitter space (AdS) is equivalent to a non-gravitational, conformal field theory (CFT) living on its boundary. This duality has opened new pathways to deal with strongly interacting quantum systems by relating it to a gravity theory. Maldacena's discovery alone was not enough to apply the holographic principle in condensed-matter systems, more advances were needed first. Gubser, Klebanov and Polyakov came to the rescue by providing a set of rules to quantitatively relate results between the two theories [34]. Witten independently came up with these rules as well [35], and hence the GKPW rule was born, which states that the partition functions of both sides are equal. These rules allow for a holographic dictionary which is incredibly useful for computations. Fast forward to more recent years and now the holographic principle is often used to deal with strongly correlated systems [23,36,37].

With the journey of the holographic principle in the back of our mind we now move on to a more mathematical explanation of the duality. Firstly, why is it called the gauge/gravity duality? Gravity stands for the bulk gravitational theory in the Anti-de Sitter space, while gauge refers to the gauge theory on its boundary. The Anti-de Sitter space is a solution to Einstein's field equations with a

negative cosmological constant [38]. The physics of the boundary is described by a conformal field theory which is located at $r \to \infty$. Here, r is the additional space coordinate of the bulk spacetime. A conformal field theory is a theory that is invariant under transformations that preserve angles. The correspondence is between the generating functional of the CFT and the partition function of the bulk theory. To be more precise, the generating functional of the CFT with source h_i for the single-trace operator $\mathcal{O}_i$ is equal to the bulk partition function with the bulk field ϕ_i, with the boundary value (at $r \to \infty$) equal to the source h_i, formulated in an equation as

$$\mathcal{Z}_{grav}(\{h_i(x)\}) = \mathcal{Z}_{QFT}(\{h_i(x)\}).\tag{4.1}$$

There are many good books and other resources that dive deeper into the intricacies of the duality [21, 30, 39], in the meantime we focus on how the condensed-matter physicist utilizes the results.

For our purposes we use the fact that we can map strongly-coupled non-gravitational physics to a weakly coupled perturbative gravity problem [39]. In practice, the correspondence is used by analyzing the bulk theory to obtain an expression for the retarded Green's functions of the boundary theory. The starting point is then the action of the bulk gravity theory. The background solutions of this action define the equilibrium properties of the boundary theory. To study the response of the field theory to small perturbations we consider fluctuations of the classical fields in the bulk on top of the background solution. This ultimately gives us a coupled set of equations. According to the holographic dictionary [21, 30, 39, 40], finding such a solution with infalling-wave boundary conditions at the black hole horizon allows us to extract all the retarded Green's functions of the system. These in-falling-wave boundary conditions essentially mean that energy is carried towards the black hole instead of emerging from it, which makes sense physically.

4.2 Gubser-Rocha model

The specific holographic model used in this thesis is called the Gubser-Rocha model [22]. Why do we use the Gubser-Rocha model? Well, one of the reasons is the fact that the background solutions to the equations of motion can be computed analytically, which means we have to perform less numerical calculations to obtain the desired results.

Secondly, the Gubser-Rocha model contains a scalar field called the dilation, such that in the low-energy theory that emerges the dynamical critical exponent $z = \infty$ and the hyperscaling violation exponent $\theta = -\infty$ both diverge, but their ratio is fixed to -1. This exact ratio ensures that the entropy scales with temperature, which in turn means that we obtain the desired linear-in-T resistivity of the strange metal.

Furthermore, the Gubser-Rocha model has been used to successfully describe certain experiments. The model is dual to a quantum field theory characterized by 'semi-local' quantum-critical behavior, which implies that the only momentum dependence in the electron self-energy is in the exponent, i.e., $\hbar\Sigma(\omega, \mathbf{k}) \propto \omega(-\omega^2)^{\nu_k - 1/2}$. It represents a quantum-critical theory because the correlation length diverges and its dynamical exponent obeys $z = \infty$. The significance of this result is that it agrees with experimental observations. For example, upon tuning the adjustable parameters in the holographic model such that $\nu_{k_F} \equiv \alpha$, this self-energy can reproduce the 'power-law liquid' model, $\hbar\Sigma''(\omega, \mathbf{k}) \propto \omega^{2\alpha}$, which very accurately describes the experimentally observed electron self-energy in ARPES measurements near the Fermi surface in the nodal direction [41]. There is even another, more recent, ARPES experiment that confirms the momentum dependence in the exponent and shows that it can accurately describe the deviations from the 'power-law liquid' model away from the Fermi surface [23]. These experiments thus indicate that the Gubser-Rocha model describes

some aspects of the strange-metal phase, although there are other properties of the strange metal that might not yet be accurately described by this model. For example, the anomalous scaling of the Hall angle [29–31]. Although this quantity is not relevant for this thesis as we consider no external magnetic field, we are aware that there might be need for a more advanced model which could describe all of these properties simultaneously.

Next, we give the gravitational action for the model [37]

$$S_{GR} = S_{ct} + \frac{c^4}{16\pi G} \int dr dt d^2x \sqrt{-g} \left[R - \frac{(\partial_\mu \phi)^2}{2} + \frac{6}{L^2} \cosh\left(\frac{\phi}{\sqrt{3}}\right) - \frac{e^{\phi/\sqrt{3}}}{4 g_F^2} F_{\mu\nu} F^{\mu\nu} \right], \quad (4.2)$$

where r is the additional spatial dimension of the bulk spacetime, g is the determinant of the metric tensor, R is the Ricci scalar and ϕ is the aforementioned dimensionless scalar field known as the dilaton [42, 43]. Moreover, $F_{\mu\nu}$ is the electromagnetic field strength tensor. Its coupling constant is $g_F^2 = c^4 \tilde{\mu}_0 / 16\pi G$, with $\tilde{\mu}_0$ the dimension of a magnetic permittivity m kg C^{-2}. Then, L is the Anti-de Sitter radius, which is the radius of curvature of the AdS spacetime. Finally, S_{ct} contains the boundary counterterms that ensure that we have a well-defined boundary problem and that the theory is properly renormalized. As mentioned before, the dilaton field ϕ is responsible for being able to describe the typical strange-metal behaviour of linear-in-T resistivity and gives also a linear momentum dependence in the exponent ν_k of the correlations. We can rewrite the action into dimensionless quantities

$$\tilde{S}_{GR} = \frac{c^3 L^2}{16\pi \hbar G} \int d\tilde{r} \, d\tilde{t} \, d^2\tilde{x} \sqrt{-g} \left[R - \frac{(\partial_\mu \phi)^2}{2} + 6 \cosh\left(\frac{\phi}{\sqrt{3}}\right) - \frac{e^{\phi/\sqrt{3}}}{4} \tilde{F}_{\mu\nu}^2 \right], \quad (4.3)$$

by defining lengths in terms of L, energies in terms of $\hbar c / L$ and absorbing the gauge coupling in the gauge field, then the prefactor of the action becomes $N_G \equiv c^3 L^2 / 16\pi \hbar G$, which is related to the large-N number of species of the boundary QFT [39]. We come back to this in principle unknown constant and explain how to fix it by looking at the experimentally observed plasma frequency. The thermodynamics of the two-dimensional strange metal is described by a background solution to the following equations: the Einstein field equations for the metric $g_{\mu\nu}$, the Maxwell equations for the $U(1)$ gauge field A_μ and the Klein-Gordon equation for the dilaton field ϕ. These equations can be obtained by varying the above action

$$R_{\mu\nu} - \frac{1}{2} R g_{\mu\nu} = T_{\mu\nu}, \quad \nabla_\mu \left(e^{\phi/\sqrt{3}} F^{\mu\nu} \right) = 0,$$

$$\nabla_\mu \nabla^\mu \phi = \frac{e^{\phi/\sqrt{3}}}{4\sqrt{3}} F^2 - \frac{2\sqrt{3}}{L^2} \sinh(\phi/\sqrt{3}), \quad (4.4)$$

with the energy-momentum tensor

$$T_{\mu\nu} = \frac{1}{2} \partial_\mu \phi \partial_\nu \phi + \frac{e^{\phi/\sqrt{3}}}{2} F_\mu^{\ \sigma} F_{\nu\sigma} - g_{\mu\nu} \left(\frac{e^{\phi/\sqrt{3}}}{8} F^2 + \frac{(\partial_\sigma \phi)^2}{4} + \frac{3}{L^2} \cosh(\phi/\sqrt{3}) \right). \quad (4.5)$$

For the background the solutions to the equations of motion are function of r only. We then have a set of equations ($g_{tt} = -1/g_{rr}$, $g_{xx} = g_{yy}$, A_t, ϕ), which supports a fully analytical black-hole solution with non-zero temperature and entropy [22]. Keeping in mind our goal of computing the response functions, we also need to consider small external perturbations of this background and we have to linearize the gravitational equations around the analytical black-hole solution. Then
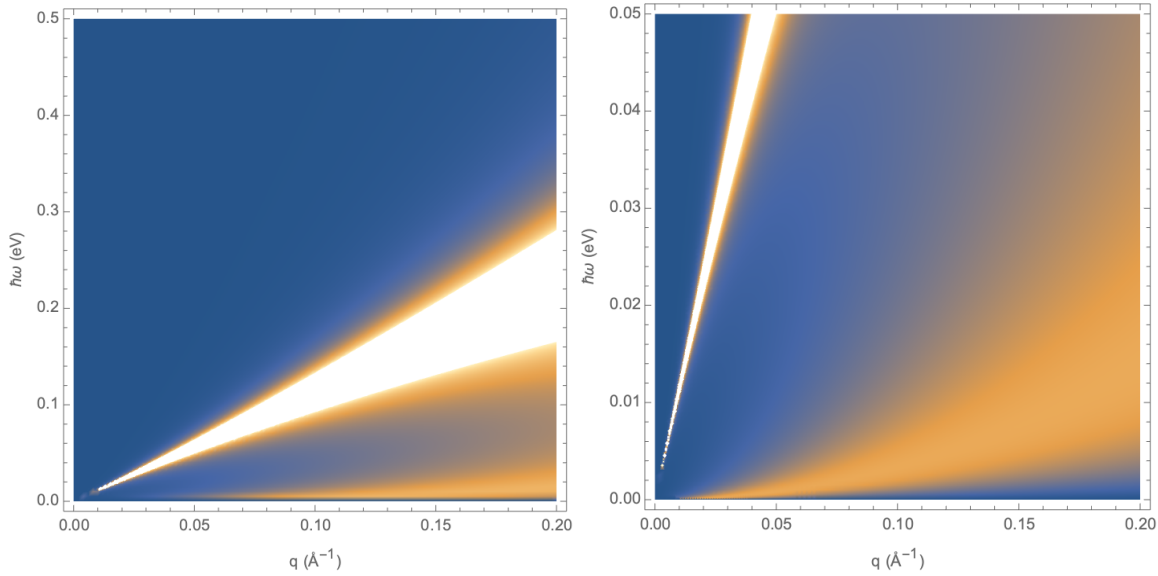
Figure 4.1: Density-density spectral function $-\Pi''$ of a single layer with only strong short-range interactions. This plot contains a linear sound mode, $\omega = v_s q$, and a diffusive mode, $\omega = -iD_d q^2$. The temperature is fixed at room temperature $T = 293$ K. In the left figure $\hbar\omega \leq 0.5$ eV and in the right figure the range of $\hbar\omega$ is decreased to more clearly display the diffusive mode.

we obtain a coupled set of equations for the fluctuations (δg_{tt}, δg_{tx}, δg_{xx}, δg_{yy}, δA_t, δA_x, $\delta\phi$) that can only be solved numerically. According to the holographic dictionary, finding a solution to the linearized equations of motion with infalling-wave boundary conditions at the black-hole horizon allows us to extract all the retarded Green's functions of the system, and thus also the desired density-density response function $\Pi(\omega, q)$, by studying the near-boundary behaviour of the field fluctuations [39].

In this manner we arrive at the objective of this section, the two-dimensional single-layer response describing the strong short-range interactions. In the low-temperature regime and at energies and momenta much smaller than the Fermi energy and Fermi momentum, respectively, we can use a hydrodynamic approximation to obtain [37, 44]

$$\Pi(\omega, q) = \frac{q^2(\omega\mathcal{D} + iv_s^2 D_d \chi q^2)}{\omega^3 + i\omega^2 q^2(2D_s + D_d) - \omega q^2 v_s^2 - iv_s^2 D_d q^4}, \tag{4.6}$$

where we have used rotational invariance to write $q \equiv |\boldsymbol{q}|$ as a scalar. In addition, $\mathcal{D}$ is the Drude weight, χ is the hydrodynamic compressibility, and we also define two diffusion constants D_s and D_d that correspond to sound diffusion and charge diffusion, respectively. Finally, v_s is the speed of sound in the material. In Section 6.2 we compute the values of these parameters.

To gain insight into the behavior of this response function the spectral function is introduced. The spectral function is defined as the imaginary part of the response function

$$-\Pi'' = -\text{Im}[\Pi]. \tag{4.7}$$

In Fig. 4.1 the spectral function is plotted with the use of variables in Eq. (4.6) typical for cuprates. In a spectral function the intensity of modes is plotted as a function of momentum and frequency
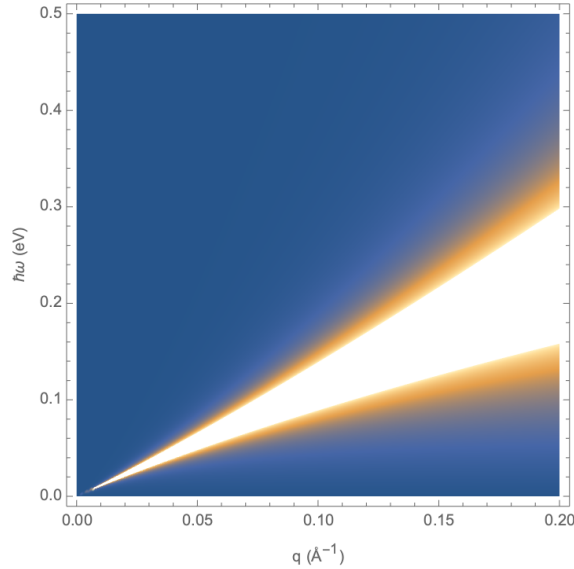
Figure 4.2: Density-density spectral function $-\Pi''$ of a single layer with only strong short-range interactions. The diffusive mode has disappeared due to the low temperature, $T = 10$ K in this plot. Only the linear sound mode, $\omega = v_s q$, remains.

or energy, thus clearly showing the associated dispersion. It also captures the broadening of the modes, which gives information about the lifetime of the modes. If the width is small the mode has a long lifetime. In Fig. 4.1 there is a linear sound mode, $\omega = v_s q$, instead of a typical plasmon mode expected in the presence of long-range Coulomb interactions and screening and with a square-root dispersion $\omega \propto \sqrt{q}$. The speed of sound is $v_s \approx 0.76 v_F = 1.14$ eV Å$/\hbar = 1.73 \times 10^5$ m s^{-1} [37]. In the limit $T = 0$ the diffusion constants vanish, as they show the same linear behavior in temperature as the resistivity, and Eq. (4.6) simplifies to

$$\Pi(\omega, q) = \frac{q^2 \mathcal{D}}{\omega^2 - v_s^2 q^2}, \tag{4.8}$$

which indeed contains the sound mode $\omega = v_s q$. This equation is used in later sections to derive the plasmon dispersion after introducing the long-range Coulomb interactions. At non-zero temperatures the density-density response function contains also a diffusive mode with $\omega = -i D_d q^2 + \mathcal{O}(q^4)$, which can be seen more clearly on the right side of Fig. 4.1.

The response function is analyzed for $\omega \ll q$, which means that in the denominator the cubed and squared terms in ω are neglected. Then multiplying both nominator and denominator with $\omega - i D_d q^2$, so as to take most easily the imaginary part, this leaves the following formula for the spectral function

$$-\Pi''(\omega, q) = \omega \, \frac{\chi - \mathcal{D}/v_s^2}{D_d q^2}, \text{ for } \omega \ll q. \tag{4.9}$$

So for small ω the intensity approaches zero linearly at a fixed value of q, confirming what is shown in Fig. 4.1. Furthermore, we see that for larger momenta the diffusive mode and the sound mode merge together.

The diffusive mode is linearly dependent on temperature, consult Section 6.2 for details, and therefore it disappears if we substantially lower the temperature, as seen in Fig. 4.2. The sound mode is unaffected and remains the same as for room temperature.

Plasmon Modes

In this chapter we finally start computing plasmon modes in the form of the density-density spectral function. They arise due to the long-range Coulomb interactions that are included. Here we treat two of the most simple geometries, starting with a single layer and thereafter placing another at a distance a.

5.1 Two-dimensional plasmons

Now that we have an appropriate response function incorporating the strong but short-range interactions in the two-dimensional strange-metal layer, long-range Coulomb interactions are introduced. We do this by coupling dynamical photons to the density current J^μ. Thus in the language of string theory we perform a so-called double-trace deformation [24, 25] of the conformal field theory. In references [36, 45] it is explained more physically how to achieve this, but in practice this means adding a boundary term to the gravitational action from Eq. (4.2) leading ultimately to

$$
\begin{aligned}
S \;=\; & \frac{1}{2} \int dt d^2x dz \int dt' d^2x' dz' J^\mu(\boldsymbol{x}, z, t) \Pi^{-1}_{\mu\nu}(\boldsymbol{x}, t; \boldsymbol{x}', t') J^\nu(\boldsymbol{x}', z', t') \\
& - \int dt d^2x dz \left(\frac{1}{4}\epsilon F_{\mu\nu} F^{\mu\nu} - e A_\mu J^\mu \right),
\end{aligned}
\tag{5.1}
$$

where z is the spatial direction orthogonal to the x-y plane and ϵ is the permittivity of the material surrounding the strange-metal layer. The addition of this boundary term does not change the linearized equations of motion, but it does change the boundary conditions for the field fluctuations [39, 46].

The current is restricted to the x-y plane where the strange-metal layer is assumed to be located, which gives the following equation for the current

$$
J^\mu(\boldsymbol{x}, z, t) = J^\mu(\boldsymbol{x}, t)\delta(z),
\tag{5.2}
$$

but let the Coulomb interactions, i.e., the photons, live in three dimensions. It is important to make this distinction because the momentum dependence of Fourier transformed Coulomb potential is different in 2D. The Fourier transform of the current is

$$
J^\mu(\omega, \boldsymbol{q}, q_z) = \int dz J^\mu(\omega, \boldsymbol{q})\delta(z)e^{-iq_z z} = J^\mu(\omega, \boldsymbol{q}).
\tag{5.3}
$$
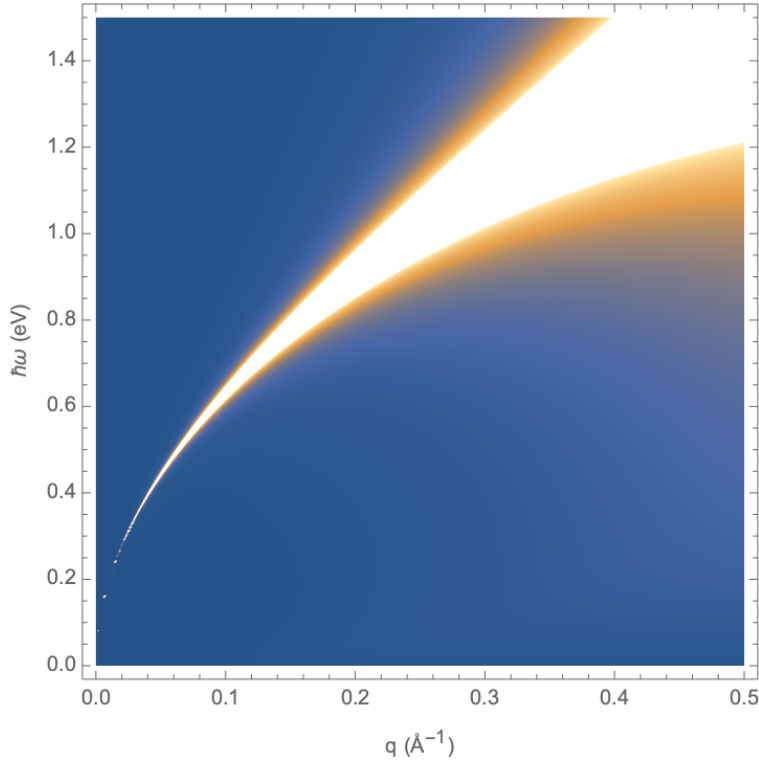
Figure 5.1: Density-density spectral function of a single layer with strong short-range interactions and long-range Coulomb interactions. We see a square-root plasmon mode in the density-density response, with $\omega \propto \sqrt{q}$. The temperature is fixed at room temperature $T = 293$ K.

It's clear that there is no dependence on q_z in the current. Note also that $\boldsymbol{q}$ is the in-plane momentum. Then we perform the double-trace deformation, Fourier transform and integrate out the photon field [36], to obtain the following action

$$S = \frac{1}{2} \int \frac{d\omega d^2q}{(2\pi)^3} \int \frac{dq_z}{2\pi} J^\mu(-\omega, -\boldsymbol{q}) \frac{\eta_{\mu\nu} e^2 / \epsilon}{q^2 + q_z^2} J^\nu(\omega, \boldsymbol{q}). \tag{5.4}$$

The next step is to integrate over q_z and also include the density-density response Π, resulting in

$$S = \frac{1}{2} \int \frac{d\omega d^2q}{(2\pi)^3} J^\mu(-\omega, -\boldsymbol{q}) \chi_{\mu\nu}^{-1} J^\nu(\omega, \boldsymbol{q}), \tag{5.5}$$

where $\chi_{\mu\nu}$ is the current-current response function and is given by

$$\chi_{\mu\nu}^{-1} \equiv \Pi_{\mu\nu}^{-1} + \frac{e^2 \eta_{\mu\nu}}{2\epsilon q}. \tag{5.6}$$

Here, χ_{00} is the density-density response, χ_{0i} is the density-current response and χ_{ij} is the current-current response.

χ_{00} is used for determining the behavior of a non-relativistic system where the velocity of the electrons is much smaller than the speed of light, $v_F \ll c$. Note that we only have an expression for Π_{00} and not for any of the other components. We substitute our expression obtained in Section 4.2,

then the density-density response function of the two-dimensional layer is

$$\chi_{00}(\omega, q) = \chi = \frac{\Pi(\omega, q)}{1 - \frac{\Pi(\omega, q)e^2}{2\epsilon q}}. \tag{5.7}$$

Thus effects of the Coulomb potential $e^2/2\epsilon q$ are obtained in a similar manner as seen in the Random-Phase Approximation (RPA) except that $\Pi(\omega, q)$ is not a non-interacting response function, but contains interaction effects via the use of the Gubser-Rocha model. Since we are dealing with a non-relativistic system, we neglect retardation effects and thus the Coulomb potential is taken independent of frequency.

In Fig. 5.1 the resulting density-density spectral function $-\chi''$ is plotted. A dispersion $\omega \propto \sqrt{q}$ is now clearly visible, as expected in a two-dimensional system. Using Eq. (4.8) the following dispersion relation is obtained

$$\omega = \sqrt{\frac{e^2 \mathcal{D}}{2\epsilon} q + v_s^2 q^2}. \tag{5.8}$$

For low momenta q this equation reduces to a square-root plasmon mode and at large q sound dispersion from the previous section is recovered. Furthermore, the width of the plasmon peak in the spectral density quickly approaches zero as the momentum approaches zero, which indicates that at long wavelengths the plasmons have a long lifetime. There is still a diffusive mode, but it is barely visible in this figure, due to the large intensity of the plasmon mode. However, the diffusion mode is essentially still the same as in the neutral response function.
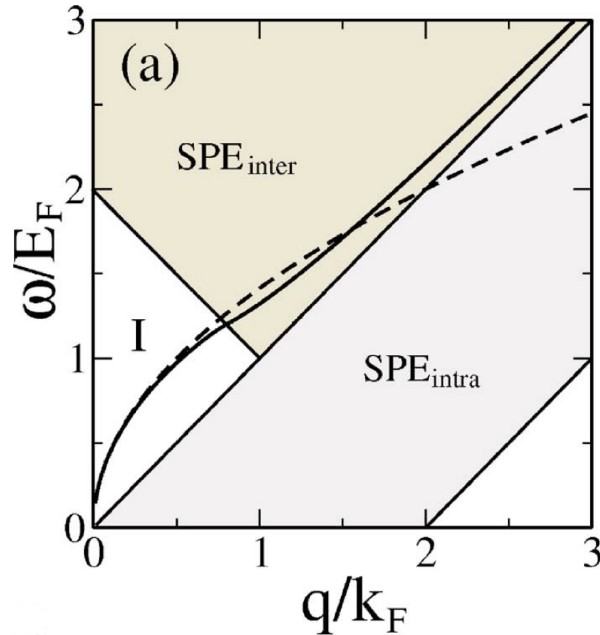
Figure 5.2: Plasmon mode dispersion, in two-dimensional graphene calculated within RPA, represented by the thick line. The plasmon mode resides in a triangle of vanishing spectral density, which is shaped by the two thin solid lines representing the inter-band and intra-band continua. Source: Fig. 1(a) of [47].

Having acquired our first spectral function, we make a comparison to a Fermi-liquid picture. We choose to compare to graphene, since the holographic approach we have made is relativistic and

because both systems are two-dimensional. The corresponding spectral function in Fig. 5.2 shows the strongly peaked plasmon mode and two continua (inter-band and intra-band). The plasmon is long-lived inside the triangle of negligible spectral density until it enters a continuum. In Fig. 5.1, however, the continuum has become widespread and the plasmon mode is always broadened and the triangle shape of zero spectral density has disappeared completely. The spreading of the continuum can be attributed to the absence of fermionic quasiparticle excitations in the holographic approach, contrary to the Fermi-liquid picture.

5.2 Bilayer plasmons

The next step after computing the plasmon modes in a single layer is stacking another layer on top at a distance a. The layers are only coupled by the long-range Coulomb interactions [48], since the strong interactions are short-range. As in the previous section the density-density response function of this bilayer system is derived. Since there are now two layers the expression for the current changes to

$$J^\mu(\boldsymbol{x},z,t) = J_1^\mu(\boldsymbol{x},t)\delta(z+a/2) + J_2^\mu(\boldsymbol{x},t)\delta(z-a/2), \tag{5.9}$$

with the indices 1 and 2 referring to each layer. This current describes two layers parallel to x-y plane separated along the z-axis by distance a. The Fourier transform of this current is given by

$$
\begin{aligned}
J^\mu(\omega,q,q_z) &= \int \frac{dz}{2\pi} \left(J_1^\mu(\omega,q)\delta(z+a/2) + J_2^\mu(\omega,q)\delta(z-a/2) \right) e^{-iq_z z} \\
&= J_1^\mu(\omega,q)e^{iq_z a/2} + J_2^\mu(\omega,q)e^{-iq_z a/2},
\end{aligned}
\tag{5.10}
$$

which is then used to compute the effective boundary action, as in the previous section

$$S = \frac{1}{2} \int \frac{d\omega d^2q}{(2\pi)^3} \int \frac{dq_z}{2\pi} \begin{pmatrix} J_1^\mu(-\omega,-\boldsymbol{q}) \\ J_2^\mu(-\omega,-\boldsymbol{q}) \end{pmatrix} \frac{\eta_{\mu\nu}e^2/\epsilon}{q^2+q_z^2} \begin{pmatrix} 1 & e^{-iq_z a} \\ e^{iq_z a} & 1 \end{pmatrix} \begin{pmatrix} J_1^\nu(\omega,\boldsymbol{q}) \\ J_2^\nu(\omega,\boldsymbol{q}) \end{pmatrix}. \tag{5.11}$$

Then the integral over q_z is worked out to obtain

$$S = \frac{1}{2} \int \frac{d\omega d^2q}{(2\pi)^3} \begin{pmatrix} J_1^\mu(-\omega,-\boldsymbol{q}) \\ J_2^\mu(-\omega,-\boldsymbol{q}) \end{pmatrix} \frac{\eta_{\mu\nu}e^2/\epsilon}{2q} \begin{pmatrix} 1 & e^{-qa} \\ e^{-qa} & 1 \end{pmatrix} \begin{pmatrix} J_1^\nu(\omega,\boldsymbol{q}) \\ J_2^\nu(\omega,\boldsymbol{q}) \end{pmatrix}. \tag{5.12}$$

Then combining this with the response function of strong short-range interactions in each layer, which we assume to be equivalent, leads to the following response function

$$S = \frac{1}{2} \int \frac{d\omega d^2q}{(2\pi)^3} \begin{pmatrix} J_1^\mu(-\omega,-\boldsymbol{q}) \\ J_2^\mu(-\omega,-\boldsymbol{q}) \end{pmatrix} \underbrace{\begin{pmatrix} \Pi_{\mu\nu}^{-1} + \frac{e^2\eta_{\mu\nu}}{2\epsilon q} & \frac{e^2\eta_{\mu\nu}e^{-qa}}{2\epsilon q} \\ \frac{e^2\eta_{\mu\nu}e^{-qa}}{2\epsilon q} & \Pi_{\mu\nu}^{-1} + \frac{e^2\eta_{\mu\nu}}{2\epsilon q} \end{pmatrix}}_{\chi_{\mu\nu}^{-1}} \begin{pmatrix} J_1^\nu(\omega,\boldsymbol{q}) \\ J_2^\nu(\omega,\boldsymbol{q}) \end{pmatrix}. \tag{5.13}$$

Now a matrix structure emerges in the response function. To analyze the matrix we take the 00-component needed to describe the condensed-matter system, as in the previous section. Then we invert the 2x2 matrix to obtain the density-density response function matrix

$$\chi_{IJ} = \frac{\Pi}{(1 - \Pi\frac{e^2}{2\epsilon q})^2 - \left(\Pi\frac{e^2}{2\epsilon q}e^{-qa}\right)^2} \begin{pmatrix} 1 - \Pi\frac{e^2}{2\epsilon q} & \Pi\frac{e^2}{2\epsilon q}e^{-qa} \\ \Pi\frac{e^2}{2\epsilon q}e^{-qa} & 1 - \Pi\frac{e^2}{2\epsilon q}, \end{pmatrix} \tag{5.14}$$
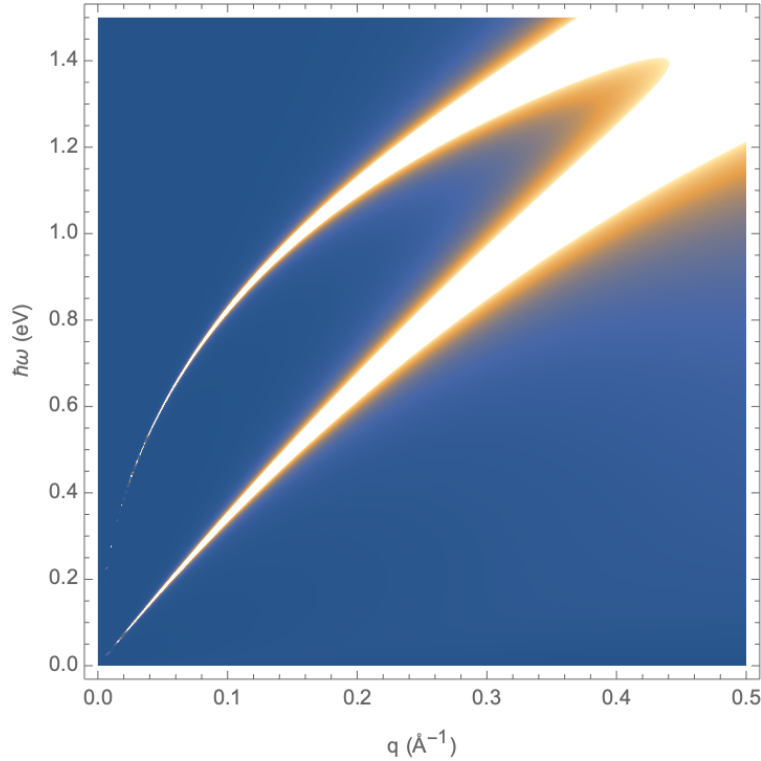
Figure 5.3: Diagonal part of the density-density spectral-function matrix of two layers with strong short-range interactions and long-range Coulomb interactions. The two layers are separated by 3.2 Å. This distance is due to the experimental setup that we model. We see the in-phase mode, $\omega \propto \sqrt{q}$, and the out-of-phase mode, $\omega \propto q$. The temperature is fixed at room temperature $T = 293$ K.

where I, J are the layer indices and thus refer to the components of the matrix. The total response function of this bilayer system is defined as $\chi \equiv \sum_{I,J} \chi_{IJ}$.

After computing the response function, we plot the diagonal part of the density-density spectral function in Fig. 5.3, i.e., $-\chi''_{II}$. The meaning of this diagonal component is that it describes the modes inside the corresponding layer and as seen in Fig. 5.3 there are two modes. One mode has in the long-wavelength limit a square-root dispersion $\omega \propto \sqrt{q}$, this is the in-phase mode, which represents oscillations inside the two layers that are in-phase, therefore the dispersion has the same form as the single-layer plasmon. The other mode displays linear dispersion $\omega \propto q$ in the long-wavelength limit and is called the out-of-phase mode, due to the oscillations being out-of-phase.

Upon substituting the zero-temperature Gubser-Rocha response the exact dispersion relations are obtained

$$\omega = \sqrt{\frac{e^2 \mathcal{D}(1 \pm e^{-qa})}{2\epsilon} q + v_s^2 q^2}. \tag{5.15}$$

The plus sign is for the in-phase mode and the minus sign is for the out-of-phase mode. Notice that in the limit $a \to \infty$, both dispersion reduces to the single-layer case, which is as expected for two uncoupled layers. Next, dispersion is expanded for small q. The dispersion of the in-phase mode is

$$\omega = \sqrt{\frac{e^2 \mathcal{D} q}{\epsilon}} + \mathcal{O}(q^{3/2}). \tag{5.16}$$

To lowest order this is similar to the single-layer dispersion. The only difference is an additional factor of two under the square root. That is because the total density is twice as big as the single-layer density, since there are two layers. In the dispersion this effectively doubles the Drude weight. For the out-of-phase mode, using the minus sign in Eq. (5.15), the following expansion of the dispersion is obtained

$$\omega = \sqrt{v_s^2 + \frac{e^2 \mathcal{D} a}{2\epsilon} q} + \mathcal{O}(q^2). \tag{5.17}$$

So the renormalized speed of sound of this mode is $\sqrt{v_s^2 + e^2 \mathcal{D} a / 2\epsilon}$. The width of this mode decreases less quickly and is wider over the whole range of q, compared to the in-phase mode. Again there is also a diffusive mode, which is not visible in this plot range because of the intensity of the plasmon modes. But it is the same as in the previous plots and has $\omega = -i D_d q^2$.
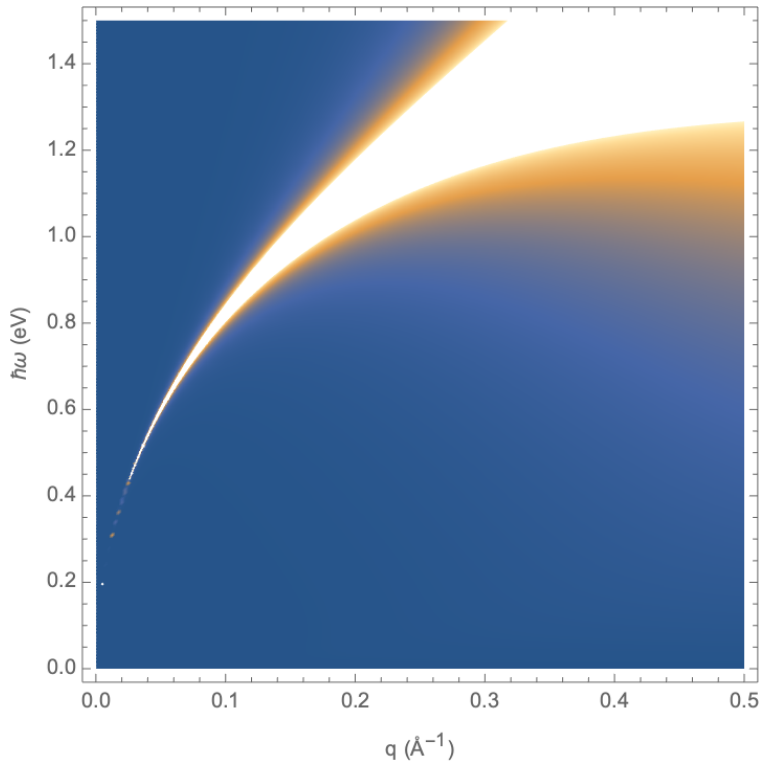
Figure 5.4: The total density-density spectral function of two layers with strong short-range interactions and long-range Coulomb interactions. The two layers are separated by 3.2 Å. This distance is due to the experimental setup that we model. Compared with Fig. 5.4 only the in-phase mode remains, $\omega \propto \sqrt{q}$. The temperature is fixed at room temperature $T = 293$ K.

Then, we also compute the total density-density response function, defined as the sum of all components of the response matrix χ_{IJ}. The total density-density spectral function $-\chi''$ is plotted in Fig. 5.4 and only contains the in-phase mode. Physically, this follows from the fact that in the total response function the out-of-phase modes from both layers cancel each other and only the in-phase behavior remains.

Layered Strange Metal

6.1 Bilayer crystal

In this chapter we arrive at the desired geometry, the bilayer crystal. We stack the bilayers treated in the previous chapter in an infinite crystal and subsequently derive the spectral function of this geometry. A unit cell of two layers is defined, with a separation of a between the two layers. Then the distance between the centers of these bilayers is defined as l. If $l = 2a$ this case reduces to a periodic crystal of single layers all separated by a. This limit is discussed in a later section. First, the appropriate Coulomb potential matrix for this layered case is derived. Thus we construct the current operator of the crystal

$$J^\mu(\boldsymbol{x}, z, t) = \sum_{n\in\mathbb{Z}} J_1^\mu(\boldsymbol{x}, z, t)\delta(z - nl + a/2) + J_2^\mu(\boldsymbol{x}, z, t)\delta(z - nl - a/2). \tag{6.1}$$

Then after Fourier transforming this expression becomes

$$J^\mu(\omega, q, q_z) = \int \frac{dz}{2\pi} \left(\sum_{n\in\mathbb{Z}} J_1^\mu(\omega, q, z)\delta(z - nl + a/2) + J_2^\mu(\omega, q, z)\delta(z - nl - a/2) \right) e^{-iq_z z}$$

$$= \sum_{n\in\mathbb{Z}} \left(J_1^\mu(\omega, q, nl)e^{iq_z a/2} + J_2^\mu(\omega, q, nl)e^{-iq_z a/2} \right) e^{-iq_z nl}. \tag{6.2}$$

Then computing the effective boundary action like in previous sections

$$\Delta S_C = \frac{1}{2} \int \frac{d\omega d^2 q}{(2\pi)^3} \int \frac{dq_z}{2\pi} \sum_{n,m} \begin{pmatrix} J_1^\mu(-\omega, -\boldsymbol{q}, nl - a/2) \\ J_2^\mu(-\omega, -\boldsymbol{q}, nl + a/2) \end{pmatrix}$$

$$\cdot \eta_{\mu\nu} \frac{e^2}{\epsilon} \frac{e^{-iq_z(n-m)l}}{q^2 + q_z^2} \begin{pmatrix} 1 & e^{-iq_z a} \\ e^{iq_z a} & 1 \end{pmatrix} \cdot \begin{pmatrix} J_1^\nu(\omega, \boldsymbol{q}, ml - a/2) \\ J_2^\nu(\omega, \boldsymbol{q}, ml + a/2) \end{pmatrix}. \tag{6.3}$$

This equation is the bilayer-crystal equivalent of Eq. (5.4). From here all the details of the derivation to the potential is given in Appendix A. We work out the integration over q_z and then Fourier transform the current, as

$$J_1^\mu(\omega, \boldsymbol{q}, nl - a/2) = (l/2\pi) \int_{-\pi/l}^{\pi/l} dp J_1^\mu(\omega, \boldsymbol{q}, p)e^{ip(nl - a/2)}. \tag{6.4}$$

Then the sum over n and m can be worked out and eventually we obtain

$$\Delta S_C = \frac{1}{2} \int \frac{d\omega d^2 q}{(2\pi)^3} \int_{-\pi/l}^{\pi/l} \frac{l dp}{2\pi} \begin{pmatrix} J_1^\mu(-\omega, -\boldsymbol{q}, -p) \\ J_2^\mu(-\omega, -\boldsymbol{q}, -p) \end{pmatrix} \cdot \frac{e^2 \eta_{\mu\nu}}{\epsilon} V(q, p) \cdot \begin{pmatrix} J_1^\nu(\omega, \boldsymbol{q}, p) \\ J_2^\nu(\omega, \boldsymbol{q}, p) \end{pmatrix}, \qquad (6.5)$$

with the following expression for the 2×2 matrix V, with the same form as for a bilayered electron-gas [49, 50],

$$V(q, p) = \frac{1}{2q(\cosh ql - \cos pl)} \begin{pmatrix} \sinh ql & (\sinh q(l-a) + e^{-ipl} \sinh qa)e^{-ipa} \\ (\sinh q(l-a) + e^{ipl} \sinh qa)e^{ipa} & \sinh ql \end{pmatrix}. \qquad (6.6)$$

Notice that the diagonal components are equal, but the off-diagonal components are each other's complex conjugate. With the potential obtained we construct the inverse of the response function as

$$\chi_{\mu\nu}^{-1} = \Pi_{\mu\nu}^{-1} + \frac{e^2 \eta_{\mu\nu}}{\epsilon} V, \qquad (6.7)$$

where the holographic response function is multiplied by the 2×2 identity matrix. For the same reason as in Chapter 5 we take the 00-component, such that the density-density response matrix is

$$\chi_{IJ} = \left[\frac{1}{\Pi} \begin{pmatrix} 1 & 0 \\ 0 & 1 \end{pmatrix} - \frac{e^2}{\epsilon} V \right]^{-1}. \qquad (6.8)$$

The diagonal part of the density-density spectral-function matrix, $-\chi_{II}''$, is plotted in Fig. 6.1 for multiple values for the Bloch momentum p. Each plot reveals two modes, arising from the periodicity of bilayers in the out-of-plane direction. Consequently, a periodic band structure emerges for both the in-phase and out-of-phase modes. Let's now review each individual plot, starting with Fig. 6.1(a), the case $p = 0$. Here, the in-phase mode manifests a gap at an energy level of 1.0 eV, signifying the plasma frequency ω_{pl} for Bi-2212. This is because we've plugged this plasma frequency in the response function. More on the derivation of parameters can be found in Section 6.2. For non-zero values of p the in-phase mode is not gapped anymore. In Fig. 6.1(b), $pl = \pi/50$, the in-phase mode does approach 1.0 eV for smaller momenta but ultimately bends down to zero at the longest wavelengths and obtains an acoustic character with a speed of sound that strongly depends on the Bloch momentum. Indeed, in the other subplots, for larger values of p, the mode becomes less steep for low momenta. For $p = \pi/l$, Fig. 6.1(d), the speed of sound of the in-phase mode reaches its minimum and approaches the speed of sound of the Gubser-Rocha model for the single layer. Conversely, the out-of-phase mode exhibits negligible dependence on p. This is reasonable from a physical standpoint, given the minimal Coulomb coupling between different bilayers in this scenario, owing to their charge-neutral nature. Also keep in mind that the domain of p in the spectral function is $[-\pi/l, \pi/l]$.

Then we move on to the total density-density spectral function, which is plotted in Fig. 6.2. It is defined as the sum of all components of the response matrix in Eq. (6.8). Compared with the diagonal component of the spectral-function matrix, the in-phase mode remains the same, but the behavior of the out-of-phase mode has changed drastically. Essentially, the intensity of the out-of-phase mode has acquired dependence on p, starting with vanishing intensity at $p = 0$ and reaching its maximum for $p = \pi/l$. The difference is caused by the presence of the phase factor $\exp(\pm ipa)$ in the off-diagonal elements of the bilayer-crystal potential in Eq. (6.6). The total density-density spectral function is used in later sections to define the total conductivity and the loss function.
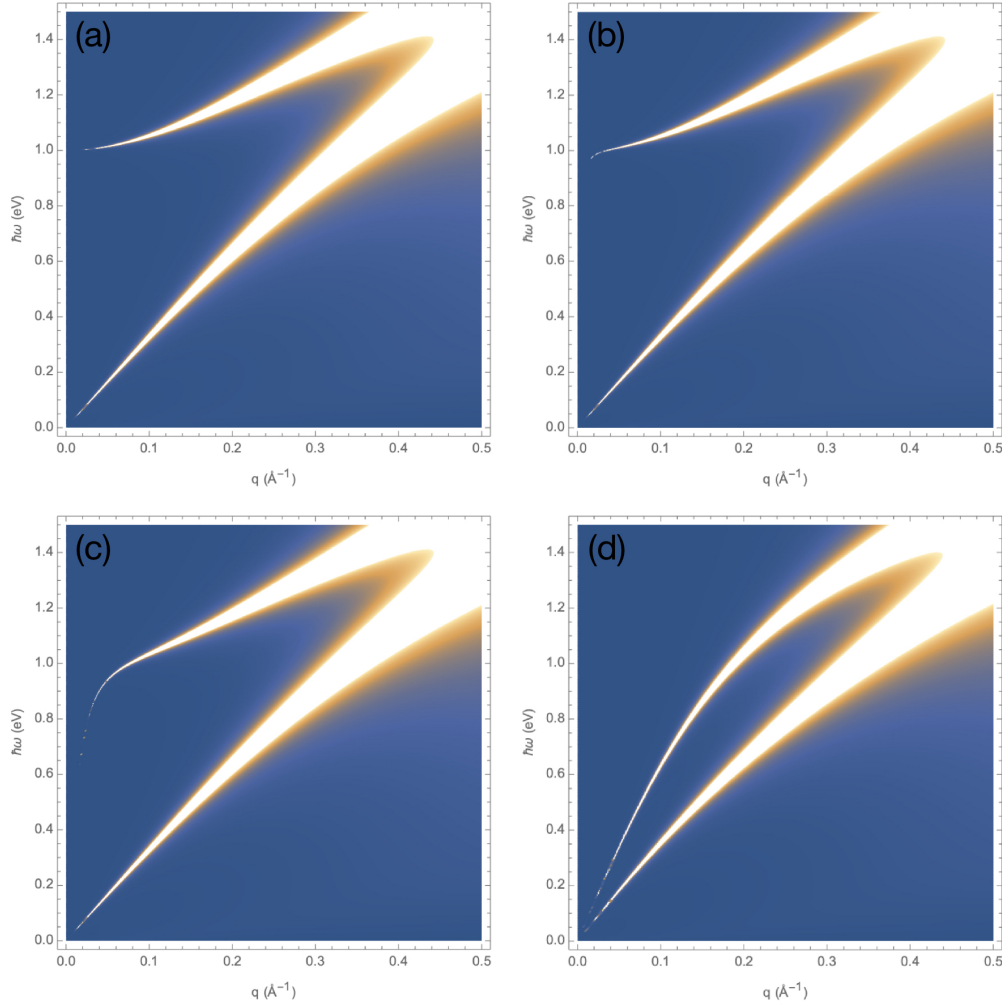
Figure 6.1: Diagonal part of the density-density spectral-function matrix of a crystal of bilayers. Each pair of layers is separated by $a = 3.2$ Å and the size of each unit cell is $l = 15.4$ Å. Each subfigure has a different value of pl. In (a), $pl = 0$, the in-phase plasmon mode is gapped as expected for a three-dimensional system and we observe in addition an out-of-phase sound mode because we have two layers per unit cell. In (b)-(d), pl is $\pi/50$, $\pi/10$ and π, respectively. Here, the out-of-phase sound mode is almost unaffected by the out-of-plane momentum p, whereas the in-phase plasmon mode is no longer gapped and has obtained also an acoustic behavior at long wavelengths. The temperature is fixed at room temperature $T = 293$ K.
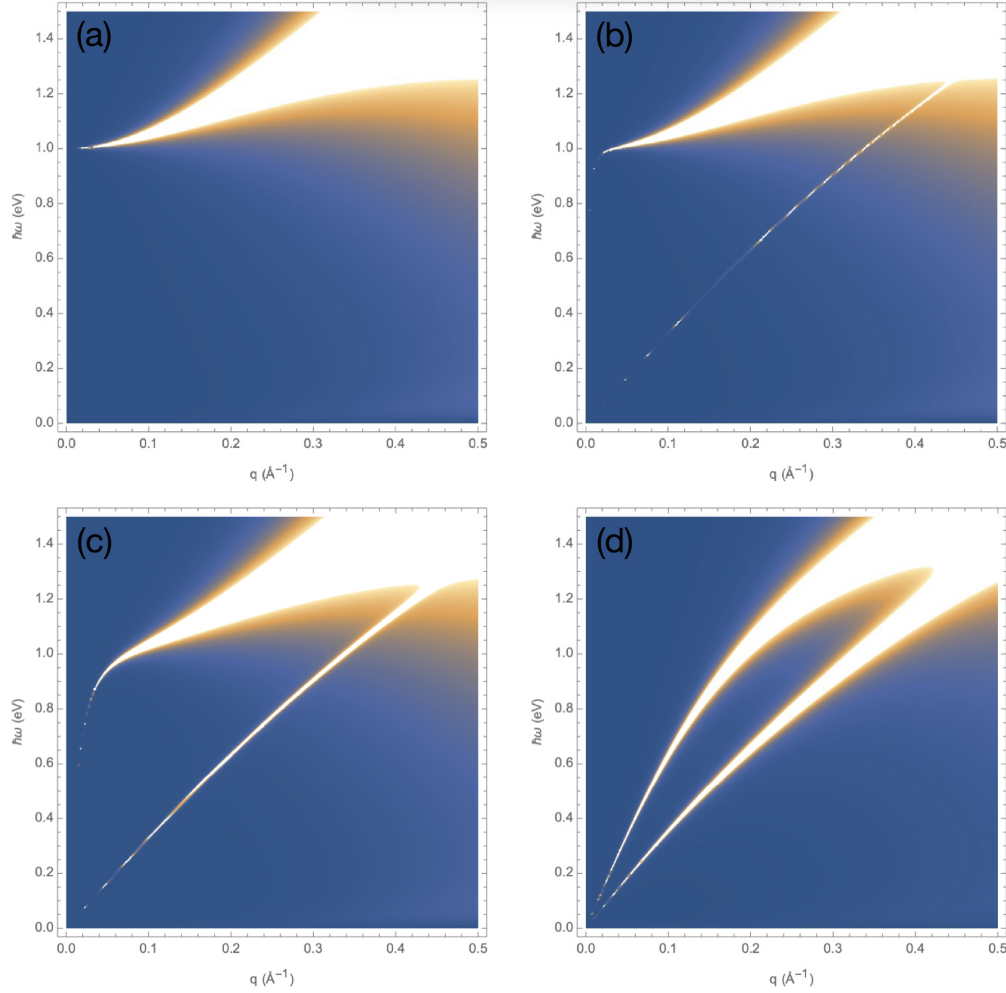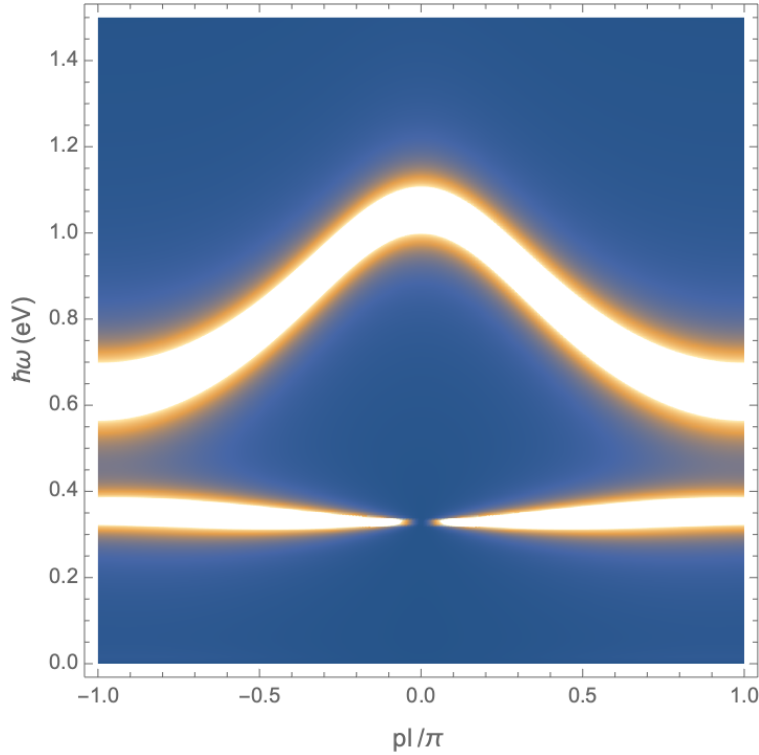
Figure 6.2: Total density-density spectral function of a crystal of bilayers. Each pair of layers is separated by $a = 3.2$ Å, and the size of each unit cell is $l = 15.4$ Å. In (a), $pl = 0$, the in-phase plasmon mode is gapped as expected for a three-dimensional system. Compared with Fig. 6.1 the out-of-phase mode is cancelled completely. In (b)-(c), pl is $\pi/50$ and $\pi/10$, respectively. Here, the out-of-phase sound mode appears, with intensity and width increasing as p increases. In (d), $pl = \pi$, the plot shows the lowest speed of sound of the in-phase mode. Furthermore, the intensity of the the out-of-phase mode reaches its maximum. The temperature is fixed at room temperature $T = 293$ K.

Another perspective of the spectral function is given by fixing q and plotting as a function of Bloch momentum p, as is done in Fig. 6.3. The increase in intensity of the out-of-phase mode is evident, as well as the limited the dispersion of this mode. The in-phase mode, however, does possess dispersion as a function of p, shaped similarly to a sine wave. The symmetry of the spectral function around $p = 0$ is clear as well.

As in previous sections the zero-temperature Gubser-Rocha response is substituted to analytically

Figure 6.3: The total density-density spectral function of a crystal of bilayers, with on the x-axis the Bloch momentum p in units of π/l. The in-plane momentum is constant at $q = 0.1 \text{ Å}^{-1}$. The dispersion of in-phase mode displays significant dependence on p, contrary to the out-of-phase, which does not display this dependence. Only the intensity of this mode is influenced by p. As mentioned previously, the out-of-phase mode vanishes for $p = 0$.

compute the dispersion. The following expression is obtained

$$\omega = \sqrt{\frac{e^2 \mathcal{D} q}{2\epsilon} \frac{\sinh ql \pm |\sinh q(l-a) + e^{ipl} \sinh qa|}{\cosh ql - \cos pl} + v_s^2 q^2}. \tag{6.9}$$

Again, the minus sign corresponds to the out-of-phase mode and the plus sign to the in-phase mode. The first thing to check is if this dispersion reduces to the bilayer case in the limit $l \to \infty$. This is indeed true, because in this limit both $\sinh ql$ and $\cosh ql$ become equal to $e^{ql}/2$ and the complicated fraction under the square root indeed exactly reproduces the result of the bilayer case in Eq. (5.15). For $p = 0$ there is a gapped mode and using the above equation we can derive an equation for the associated plasma frequency. Taking the limit $q \to 0$ for the in-phase mode and $p = 0$, results in

$$\omega_{pl} = \sqrt{\frac{2e^2 \mathcal{D}}{l\epsilon}}. \tag{6.10}$$

Here, the plasma frequency is defined in terms of the two-dimensional Drude weight $\mathcal{D}$. But can also be written in terms of the three-dimensional Drude weight $\mathcal{D}_{3D} = 2\mathcal{D}/l$, which shows that the plasma frequency equals the familiar result $\omega_{pl} = \sqrt{e^2 \mathcal{D}_{3D}/\epsilon}$. Using these equations the dispersion is rewritten as

$$\omega = \sqrt{\omega_{pl}^2 \frac{ql}{4} \frac{\sinh ql \pm |\sinh q(l-a) + e^{ipl} \sinh qa|}{\cosh ql - \cos pl} + v_s^2 q^2}, \tag{6.11}$$

from which an expression for the two speeds of sound for $p \neq 0$ follows. Namely,

$$v_{\pm}(p) = \sqrt{v_s^2 + \frac{\omega_{pl}^2 l}{4} \frac{l \pm |l + (e^{ipl} - 1)a|}{1 - \cos pl}}. \tag{6.12}$$

6.1.1 Conductivity

In this section we consider the conductivity of the bilayer crystal. First, the following formula for the total density-density response function in the long-wavelength limit is obtained

$$\lim_{q \to 0} \chi(\omega, q, p = 0) = \frac{2\mathcal{D}q^2}{\omega^2 - \omega_{pl}^2}, \tag{6.13}$$

where $\chi = \sum_{IJ} \chi_{IJ}$ is the total density-density response function of the bilayer crystal. The above expression is rewritten by factoring $i\omega$ out in the denominator, leading to

$$\chi(\omega, q, p) = \frac{2\mathcal{D}q^2}{-i\omega} \frac{1}{i\omega + \frac{\omega_{pl}^2}{i\omega}}. \tag{6.14}$$

Next, recognize that the second denominator has the form of the continuity equation for the electron density, together with both Ohm's law and Gauss's law. This can be derived as follows, start with the continuity equation

$$\frac{\partial n(x, t)}{\partial t} + \nabla \cdot j(x, t) = 0, \tag{6.15}$$

together with Ohm's law

$$j(x, t) = \sigma E, \tag{6.16}$$

and Gauss' law

$$\nabla \cdot E(x, t) = \frac{n(x, t)}{\epsilon}, \tag{6.17}$$

and then substitute a plane-wave solution, the result is

$$\left(-i\omega + \frac{\sigma(\omega)}{\epsilon}\right) n = 0, \tag{6.18}$$

which means that the conductivity is

$$\sigma(\omega) = \frac{e^2 \mathcal{D}_{3D}}{-i\omega}. \tag{6.19}$$

Note the use of the formula for the plasma frequency $\omega_{pl} = \sqrt{e^2 \mathcal{D}_{3D}/\epsilon}$. Furthermore, the same result can also be obtained directly from the 'neutral' in-plane conductivity as

$$\sigma(\omega) = \frac{2}{l} e^2 \lim_{q \to 0} \frac{i\omega}{q^2} \Pi(\omega, q) = \frac{2e^2}{l} \frac{\mathcal{D}}{-i\omega}, \tag{6.20}$$

which is as expected physically since Coulomb interactions do not affect the acceleration of the total momentum due to the applied electric field. At this point the real part of the above expression leads to a delta function centered around $\omega = 0$, signaling the absence of momentum relaxation in our theory. But in an experiment there is typically disorder in the sample. This disorder can

be incorporated using the Planckian dissipation appropriate for the cuprates [51], by performing the replacement $\omega \to \omega + \frac{i}{\tau}$ in the right-hand side. Planckian dissipation gives the following expression for the relaxation time τ

$$\frac{\hbar}{\tau} = \alpha k_B T, \tag{6.21}$$

with α a material parameter. For Bi-2212, it is approximately 1.1 ± 0.3 [51]. The fact that the dissipation rate is linear in temperature aligns with the fact that the diffusion constants in the strong short-range response function are also linear in temperature. So this is consistent with the use of the Gubser-Rocha model for the strange-metal phase. After introducing Planckian dissipation in the above manner, Eq. (6.19) becomes

$$\sigma(\omega, \tau) = \frac{e^2 \mathcal{D}_{3D}}{-i\omega + 1/\tau}, \tag{6.22}$$

displaying the Drude form with the dc-conductivity inversely proportional to temperature. Consequently, the resistivity is linear in temperature, as required for strange metals.
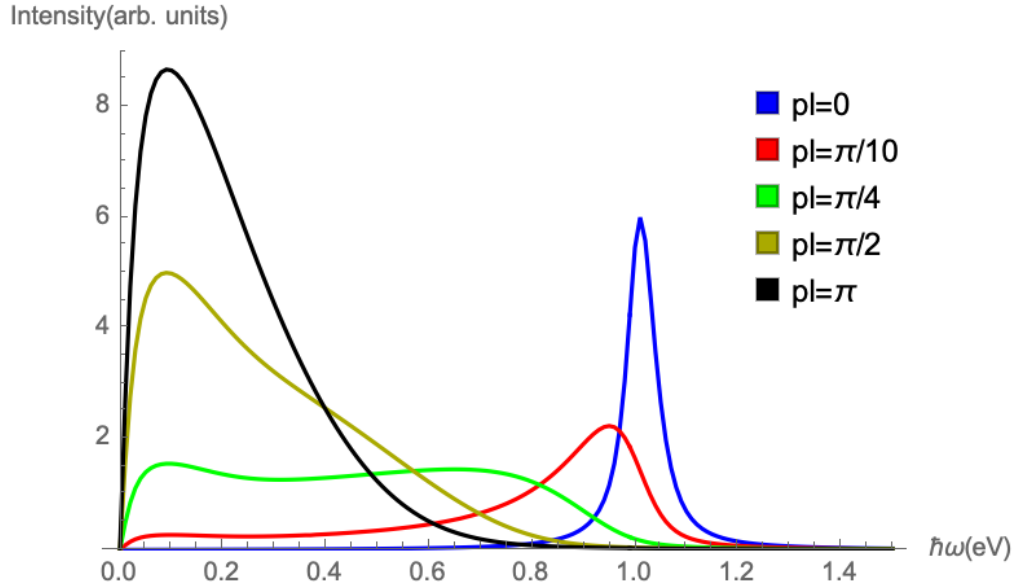
6.1.2 Loss function

With the proper modelling of disorder in the cuprates determined we are now able to compute the loss function, which can be measured in transmission electron energy loss spectroscopy (EELS) experiments. Another aspect to take into account is the beam resolution that comes with performing an experiment. The in-plane momentum resolution is incorporated in the experiments by defining the following average loss function

$$L(\omega, q_0, p) = \frac{2}{\Delta q^2} \frac{1}{e^{-\left(\frac{q_0}{\Delta q}\right)^2} + \sqrt{\pi} \frac{q_0}{\Delta q} \left(1 + \mathrm{erf} \frac{q_0}{\Delta q}\right)} \int_0^\infty dq q e^{-\left(\frac{q-q_0}{\Delta q}\right)^2} \mathrm{Im}\left[-\frac{\chi(\omega + \frac{i}{\tau}, q, p)}{q^2}\right]. \tag{6.23}$$

In this formula χ is again the total density-density response function of the bilayer crystal, and we take the imaginary part, which shows that transmission EELS measures essentially the density-density spectral function. We have incorporated disorder in the same fashion as in the previous section, using Planckian dissipation, and performed the replacement $\omega \to \omega + \frac{i}{\tau}$. Then we average with a Gaussian distribution centered around q_0, denoting the measured in-plane momentum transfer, and with a width Δq that represents the experimental momentum resolution. The factor in front of the integral acts as a normalization such that the intensity of the loss function can be compared across a range of in-plane momentum.

In Fig. 6.4 the loss function $L(\omega, q_0, p)$ is plotted for $q_0 = 0$ and $\Delta q = 0.05 \text{ Å}^{-1}$. For these parameters the loss function exhibits a pronounced dependence on p. The blue graph, $pl = 0$, has its peak at around 1.0 eV. Then as p increases the peak widens and decreases in intensity, as seen for $pl = \pi/4$. In this case no discernible peak is left and the loss function has become incredibly broad. Upon increasing p further a new peak appears around 0.15 eV, which corresponds approximately to $2\hbar v_s \Delta q$ for $pl = \pi$. The behavior on display in this figure can be explained by consulting the total density-density spectral function of Fig. 6.2. Namely, as p is increased the spectral weight moves towards lower energies, especially because we take $q_0 = 0$ in this case and this mirrors what we see in the loss function. The main difference is the width of the peaks, which is caused by the Planckian dissipation included in the loss function.
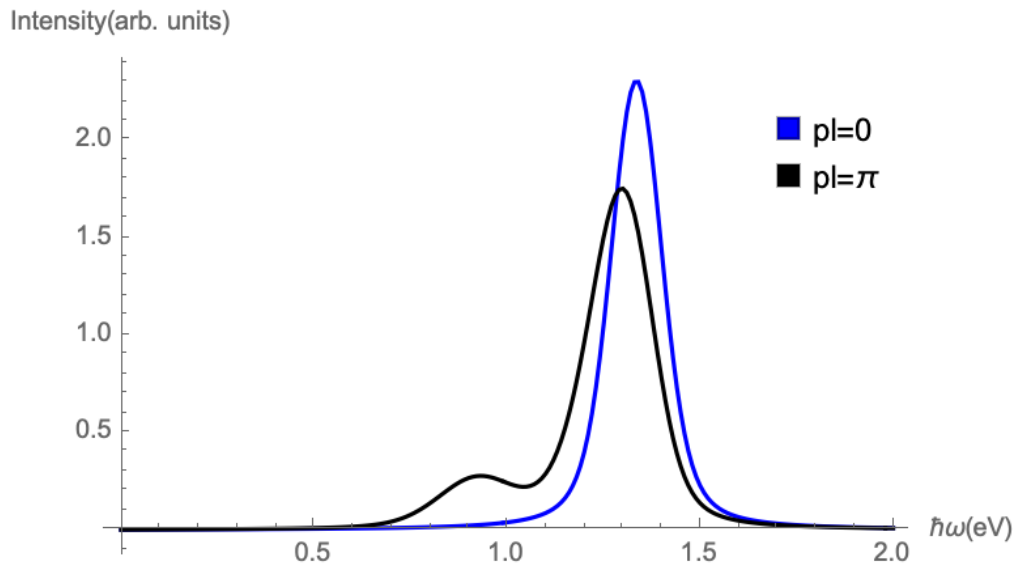
Figure 6.4: The loss function for $q_0 = 0$. The uncertainty is characterized by $\Delta q = 0.05$ Å^{-1}. Multiple values of p are used, indicated in the legends, and we also describe Planckian dissipation with $\alpha = 1.1$. There is strong p dependence in this case.

In Fig. 6.5 the in-plane momentum is raised to $q_0 = 0.3$ Å^{-1}, with consequence that the p dependence has almost disappeared. For clarity's sake, only the two outermost values are plotted. The energy of the plasmon peak for $p = 0$ has increased to around 1.35 eV. Meanwhile, the main peak of intensity for $pl = \pi$ has shifted to 1.3 eV and second peak has appeared, which can be attributed to the out-of-phase mode. Once again, looking back at the bilayer-crystal spectral function of Fig. 6.2, it is clear that dependence on Bloch momentum p decreases for larger in-plane momentum.

In these plots we have assumed a single value of p, but an experiment could also have uncertainty in the out-of-plane momentum p, so we introduce also Δp to model this but always centered at $p_0 = 0$. For us, the case of $p_0 = 0$ is most relevant but this can be easily extended to any p_0. This leads to our final average loss function

$$L(\omega, q_0) = \frac{2}{\sqrt{\pi}\Delta p} \int_0^\infty dp\, e^{-\left(\frac{p}{\Delta p}\right)^2} L(\omega, q_0, p). \tag{6.24}$$

We have plotted this in Fig. 6.6 and we see that for smaller uncertainty Δp only the 1.0 eV is visible, while for larger uncertainty in p there are contributions from both small and large p. Such that there are two peaks in the loss function. This is not due to the fact that there are two modes, but due to the p dependence of the plasmon mode. We especially display this for $q_0 = 0$, because this is a value of the in-plane momentum with a great dependence on p. For larger in-plane momenta the uncertainty in p does not make a significant difference.

Figure 6.5: The loss function for $q_0 = 0.3\ \text{Å}^{-1}$. The uncertainty is characterized by $\Delta q = 0.05\ \text{Å}^{-1}$. Multiple values of p are used, indicated in the legends and we also include Planckian dissipation with $\alpha = 1.1$. Compared with Fig. 6.4 there is little dependence on p. We have only plotted the outermost values of p, to make the figure more clear. We also observe that the energy of the peak has increased compared to Fig. 6.4. The smaller peak visible for $pl = \pi$ is due to the out-of-phase mode.
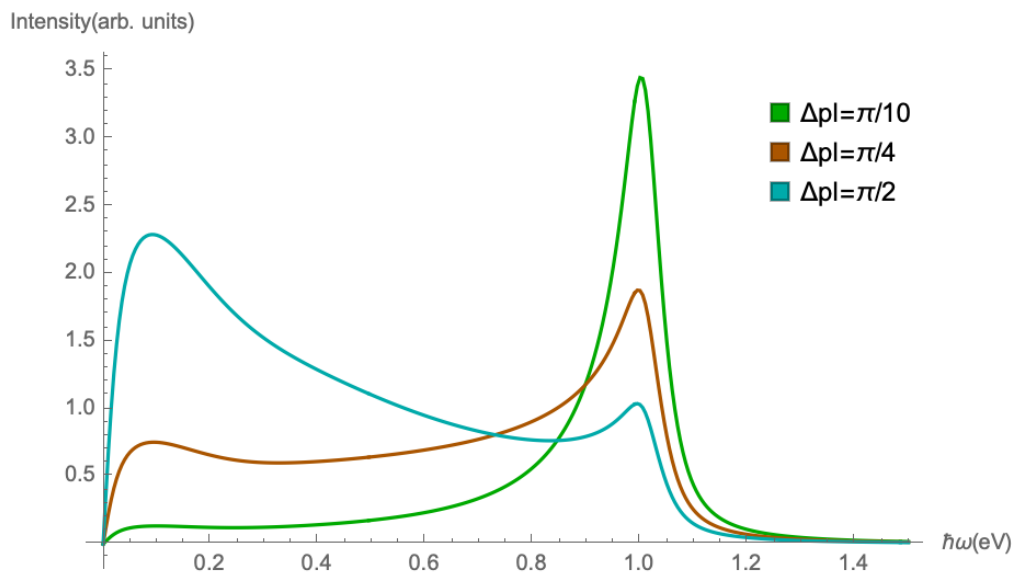
Figure 6.6: The dependence of the average loss function on the out-of-plane momentum resolution for $q_0 = 0$, $\Delta q = 0.05\ \text{Å}^{-1}$, $p_0 = 0$, and $\alpha = 1.1$.

6.1.3 Umklapp scattering

In this section we introduce anisotropy in the CuO_2 layers by incorporating Umklapp scattering, a process in which charge carriers scatter off a periodicity in the layers [52, 53]. We compute the response function and display the results in the spectral function and loss function.

The model used until now is rotationally invariant around the z-axis of the material, since we assume the in-plane rotational invariance. However, there is a square lattice in the CuO_2 layers which breaks the rotational symmetry. Furthermore, in Bi-2212 there is a certain periodicity of approximately 4.7 in the direction 45 degrees rotated from the lattice in reciprocal space [33]. In the literature this periodicity is called supermodulation. This can be seen in the diffraction pattern of the sample [26]. Since we are interested in the long-wavelength physics of the cuprates incorporating the shorter period of the supermodulation is preferred over incorporating lattice sites themselves.

We introduce Umklapp scattering by rewriting the expression for the density fluctuations in real space

$$n(x) = \sum_q \left(n_{q+q'} e^{i(q+q')\cdot x} + n_q e^{iq\cdot x} + n_{q-q'} e^{i(q-q')\cdot x} \right), \tag{6.25}$$

where the vector $q' = (2\pi/4.7b, 0)$, with $b = 5.31$ Å. This quantity is the in-plane lattice unit, equal to $\sqrt{2}$ times the distance between nearest copper atoms in the CuO_2 planes. The definition of q' is such that the x-direction is taken as the direction of the supermodulation. We take only the two nearest "neighbors" into account, since these have the most impact at long wavelengths.

We assume that these modes only couple to the main mode and not to each other. The strength of the coupling is characterized by g, which results in the following expression,

$$S = \int d^4x \left(\int d^4x' n(x) \chi(x-x')^{-1} n(x') + g n^2(x) \cos(q'x) \right). \tag{6.26}$$

Upon Fourier transforming this expression we obtain a matrix structure. On the diagonal we have the density-density response function of the bilayer crystal with the momentum offset by q'. Furthermore, we have coupling matrices g_{IJ} on the center column and row. Concretely, we obtain

$$\begin{pmatrix} n_{I,-q+q'} \\ n_{I,-q} \\ n_{I,-q-q'} \end{pmatrix} \begin{pmatrix} \chi_{IJ}^{-1}(q-q') & g_{IJ} & 0 \\ g_{IJ} & \chi_{IJ}^{-1}(q) & g_{IJ} \\ 0 & g_{IJ} & \chi_{IJ}^{-1}(q+q') \end{pmatrix} \begin{pmatrix} n_{J,q-q'} \\ n_{J,q} \\ n_{J,q+q'} \end{pmatrix}.$$

The indices I, J indicate in which layer the density fluctuation is. This is because there is no Umklapp scattering between two separate layers. Therefore, the matrix g_{IJ} is the 2×2 identity matrix. χ_{IJ} is the density-density response matrix for the bilayer crystal. We want to describe the density fluctuations for momentum q, which means we need to solve for n_q. Thus we obtain the density-density response function that describes the Umklapp scattering,

$$X(q,\omega) = \sum_{I,J} \left[\chi_{IJ}^{-1}(q,\omega) - g^2 \left(\chi_{IJ}(q+q',\omega) + \chi_{IJ}(q-q',\omega) \right) \right]^{-1}, \tag{6.27}$$

where X is the total density-density response function including Umklapp scattering. When the coupling is zero, this equation reduces to the total density-density response function without Umklapp scattering, as expected.

The density-density spectral function is plotted in Fig. 6.7, showing the effect that the Umklapp processes have on the plasmon modes. In this figure the in-plane momentum is taken in the
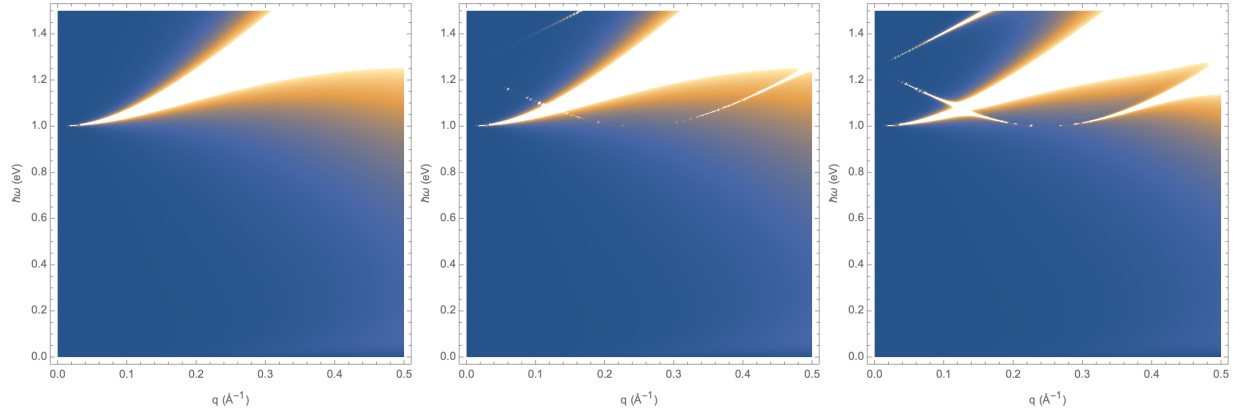
Figure 6.7: The total density-density spectral function $-X''$ in the q_x direction for $p = 0$. From left to right $g = 0, 1, 10$. For this value of p there is no out-of-phase mode.
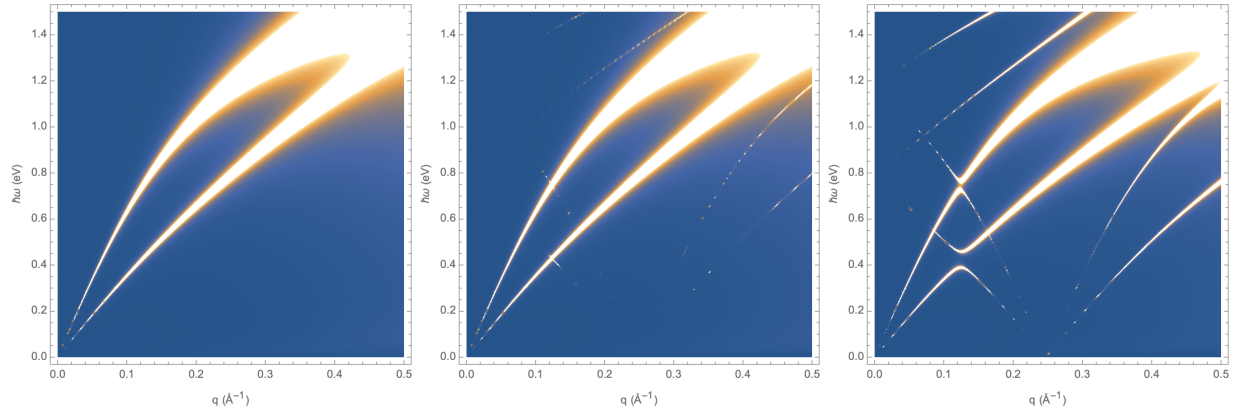

Figure 6.8: The total density-density spectral function $-X''$ in the q_x direction for $p = \frac{\pi}{l}$. From left to right $g = 0, 1, 10$. For this value of p the out-of-phase mode is at its maximum intensity.

direction of the supermodulation. Out-of-plane momentum p equals 0, which means that only the in-phase mode is visible. Upon turning the Umklapp scattering on there appear two more modes in the figure. They emanate from $q = \frac{2\pi}{4.7b} \approx 0.25$ Å^{-1}, due to the period of the supermodulation. For $g = 1$ these modes are very low intensity, while at $g = 10$ the intensity increases and an avoided crossing becomes visible at approximately $q = 0.1$ Å^{-1}.

Then in Fig. 6.8 the out-of-plane momentum p is increased to $\frac{\pi}{l}$, which means that the intensity of the out-of-phase mode is now significant compared to the in-phase mode. It is clear that the Umklapp scattering has much more impact on the spectral function for $p = \frac{\pi}{l}$. Namely, there are two clearly visible avoided crossings for $g = 10$. Furthermore, there are modes which emanate from zero energy at $q = \frac{2\pi}{4.7b} \approx 0.25$ Å^{-1}.

The natural next step is to compute the loss function, since it allows us to see more clearly what the effects of Umklapp scattering are for experimental setups. As in the previous section we include Planckian dissipation to account for impurities.

In Fig. 6.9 the loss function is plotted for $q_x = 0.3$ Å^{-1}, which is in the direction of the supermodulation. $p = 0.3$ Å^{-1} is taken, due to fact that in EELS experiments the in-plane and out-of-plane
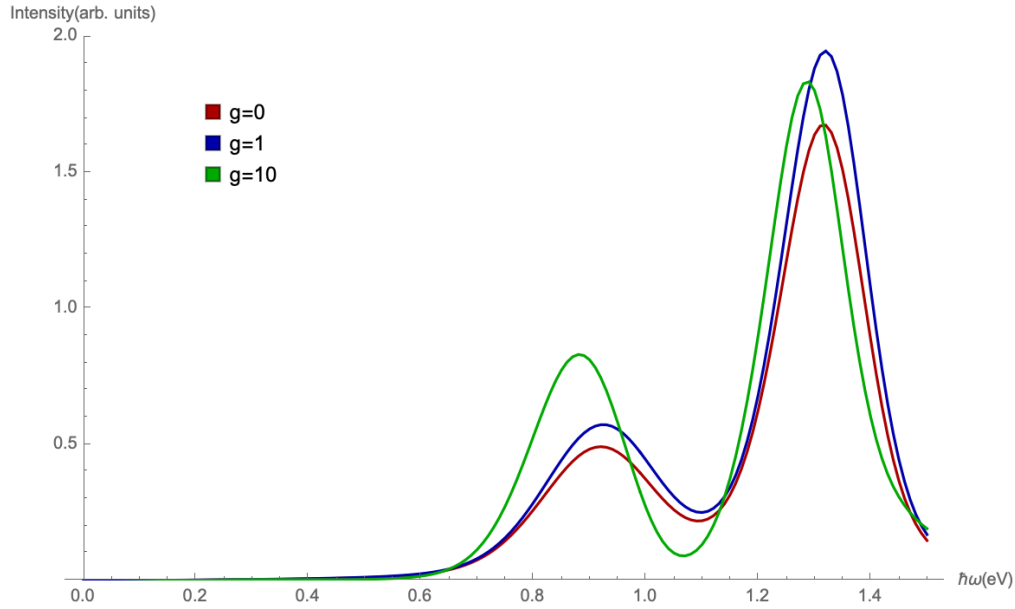
Figure 6.9: Loss function for $(q_x, q_y) = (0.3, 0)$ Å^{-1} and $p = 0.3$ Å^{-1} with uncertainty in p and q equal to 0.05 Å^{-1}. The direction of the supermodulation is defined as q_x. The intensity of the plots for $g = 1$ and $g = 10$ have been amplified such that their intensity is comparable with the $g = 0$ case. Therefore, comparing intensities across different values of g is not possible.

momentum are assumed to be equal. Since this value is outside of $[-\pi/l, \pi/l]$, it is the same as taking the value minus $2\pi/l$, then $p \approx -0.108$. Since the spectral function is an even function of p, the value of $p = 0.108$ delivers the exact same behavior of the loss function.

In the red plot, $g = 0$, there are two peaks visible. The greatest peak is at around 1.3 eV and the smaller peak is at around 0.9 eV. For the $g = 1$ curve there has not changed much compared with $g = 0$. Then for $g = 10$ both peaks have lower energy.

Then in Fig. 6.10 the loss function is plotted in the direction rotated 45 degrees from the supermodulation. Compared with Fig. 6.9 the $g = 10$ case is now much more similar to the $g = 0$ case. It seems that there is less effect from Umklapp scattering at this point in momentum space.

In Fig. 6.11 the loss function is now plotted for the in-plane momentum direction perpendicular to the supermodulation. The $g = 0$ curve is still the same as in Fig. 6.9, since there is in-plane rotational symmetry in that case, but in contrast the $g = 10$ plot has changed. Comparing this plot with Fig. 6.9 the energy of the lower energy peak has moved to approximately 0.8 eV and the higher energy peak has moved to 1.25 eV. Remarkably, in between these two peaks the loss function approaches zero intensity. It seems that the Umklapp scattering has caused more separation between the two modes.

To summarize, new modes, with low intensity, are created due to Umklapp scattering. They cause avoided crossings, which are visible in the spectral function. And in the loss function the new modes lower the energies of the plasmon peaks. Furthermore, the rotational invariance is destroyed and replaced by a periodicity of 180 degrees.
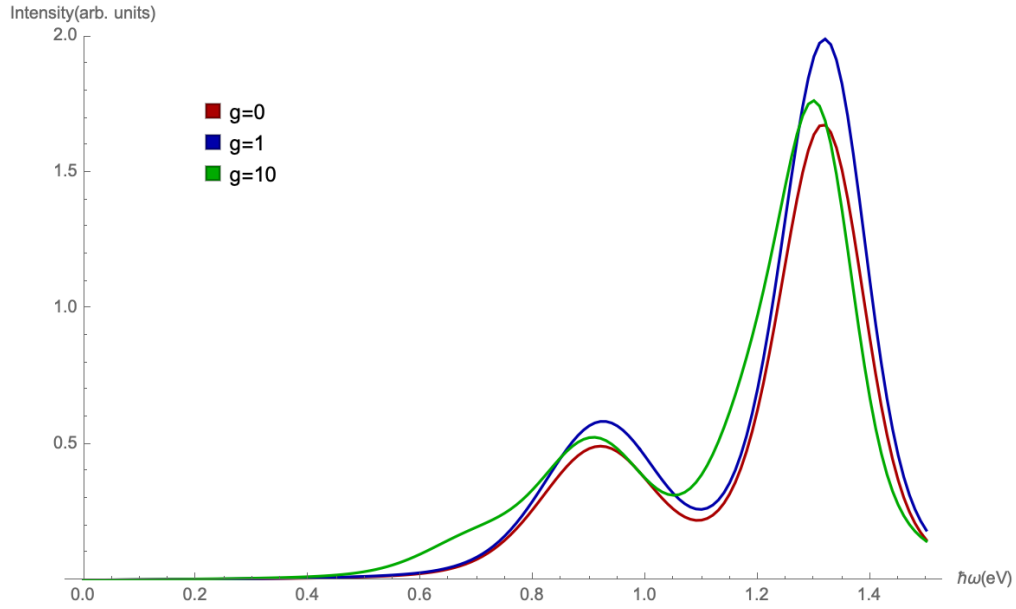
Figure 6.10: Loss function for $(q_x, q_y) = \frac{1}{\sqrt{2}}(0.3, 0.3)$ Å^{-1} and $p = 0.3$ Å^{-1} with uncertainty in p and q equal to 0.05 Å^{-1}. This plot is in the direction 45 degrees rotated from the supermodulation. The intensity of the plots for $g = 1$ and $g = 10$ have been amplified such that their intensity is comparable with the $g = 0$ case. Therefore, comparing intensities across different values of g is not possible.
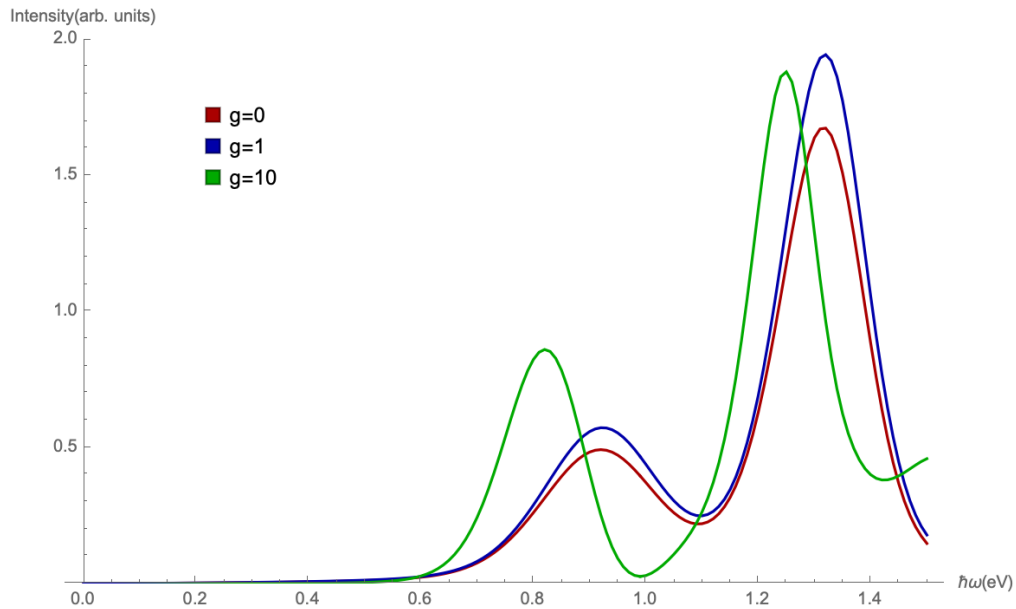
Figure 6.11: Loss function for $(q_x, q_y) = (0, 0.3)$ Å^{-1} and $p = 0.3$ Å^{-1} with uncertainty in p and q equal to 0.05 Å^{-1}. This plot is in the direction perpendicular to the supermodulation. The intensity of the plots for $g = 1$ and $g = 10$ have been amplified such that their intensity is comparable with the $g = 0$ case. Therefore, comparing intensities across different values of g is not possible.
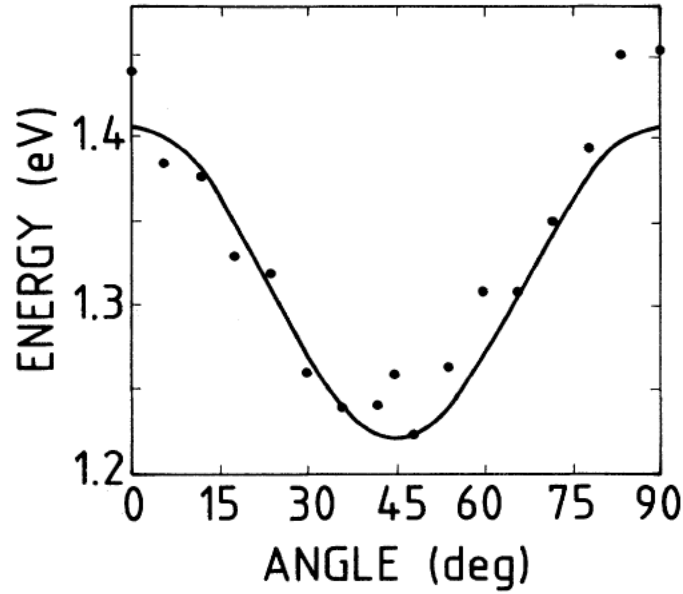
Figure 6.12: Plasmon energy measured in Bi-2212 by Nücker et al. For constant in-plane momentum $q = 0.3$ Å^{-1}. Here, 0 degrees indicates the nodal direction of the cuprate. Source: [13].

The angular dependence of the plasmon mode has been researched in the past. For example, the optical plasmon was measured by Nücker et al [13]. They measured for in-plane momentum $q = 0.3$ Å^{-1} and obtained a periodicity of 90 degrees. But since supermodulation is only in one direction, it gives a periodicity of 180 degrees. Therefore, supermodulation can never cause the pattern observed in Fig. 6.12. Evidently, this calls for another explanation and deserves more attention in the future.

6.1.4 Hopping

Another feature we can implement in our model is hopping between the CuO$_2$ layers. We achieve this by adding a dispersion in the z-direction. First, we do an electron gas calculation to justify the assumption that will be made for the density-density response function. We define

$$\epsilon'_q = \frac{\hbar^2}{2m}(q_x^2 + q_y^2 + \alpha q_z^2). \tag{6.28}$$

Here x and y are the in-plane coordinates and z is the out-of-plane coordinate. The kinetic energy in the z direction is characterized by α. Then compute the bubble diagram, as in Ultracold Quantum Fields [28]

$$\hbar\Pi(q, i\omega_n) \equiv \frac{1}{\hbar\beta}\sum_{n'}\int\frac{d\boldsymbol{q}'}{(2\pi)^3}G^H(\boldsymbol{q}+\boldsymbol{q}', i\omega_n + i\omega_{n'})G^H(\boldsymbol{q}', i\omega_{n'}), \tag{6.29}$$

with the following expression for the Green's function from Hartree theory

$$G^H(\boldsymbol{q}, i\omega_n) = \frac{-\hbar}{-i\hbar\omega_n + \epsilon_{q'} - \mu}. \tag{6.30}$$

The difference with the computation in UQF is that now there is anisotropy introduced in Eq. (6.28). Note that the expression for bubble diagram is the density-density response function. Start with

$$\Pi(\boldsymbol{q}, i\omega_n) = 2 \int \frac{d\boldsymbol{q'}}{(2\pi)^3} \frac{N_{FD}(\epsilon'_{q+q'}) - N_{FD}(\epsilon'_{q'})}{\epsilon'_{q+q'} - \epsilon'_{q'} - i\hbar\omega_n}. \tag{6.31}$$

Then expanding the Fermi distribution N_{FD} around $\boldsymbol{q} = \boldsymbol{0}$, we obtain

$$N_{FD}(\epsilon'_{q+q'}) = N_{FD}(\epsilon'_{q'}) + \frac{\partial N(\epsilon)}{\partial \boldsymbol{q'}} \cdot \boldsymbol{q} + \mathcal{O}(q^2) \tag{6.32}$$

$$= N_{FD}(\epsilon'_{q'}) + \frac{\partial N(\epsilon)}{\partial \epsilon}\bigg|_{\epsilon=\epsilon'_{q'}} \times \frac{\hbar^2}{m} \begin{pmatrix} q'_x \\ q'_y \\ \alpha q'_z \end{pmatrix} \cdot \boldsymbol{q} + \mathcal{O}(q^2). \tag{6.33}$$

Having obtained this expression Eq. (6.31) can be simplified to obtain

$$\Pi(\boldsymbol{q}, \omega) \simeq 2 \int \frac{d\boldsymbol{q'}}{(2\pi)^3} \frac{\hbar^2(q'_x q_x + q'_y q_y + \alpha q'_z q_z)}{\hbar^2(q'_x q_x + q'_y q_y + \alpha q'_z q_z) - m\hbar\omega} \frac{\partial N(\epsilon)}{\partial \epsilon}\bigg|_{\epsilon=\epsilon'_{q'}}. \tag{6.34}$$

In the limit $q/\omega \to 0$, the denominator can be expanded, resulting in the following expression

$$\Pi(\boldsymbol{q}, \omega) \simeq -2 \int \frac{d\boldsymbol{q'}}{(2\pi)^3} \left(1 + \frac{\hbar^2}{m} \frac{(q'_x q_x + q'_y q_y + \alpha q'_z q_z)}{\hbar\omega}\right) \frac{\hbar^2}{m} \frac{(q'_x q_x + q'_y q_y + \alpha q'_z q_z)}{\hbar\omega} \frac{\partial N(\epsilon)}{\partial \epsilon}\bigg|_{\epsilon=\epsilon'_{q'}}. \tag{6.35}$$

The integrand linear in $\boldsymbol{q}$ is antisymmetric and thus vanishes upon integration. For the quadratic term the observation that the derivative of the Fermi distribution is strongly peaked around the chemical potential is used. Therefore this can be approximated to a delta function

$$\frac{\partial N_{FD}(\epsilon)}{\partial \epsilon} \simeq -\delta(\mu - \epsilon). \tag{6.36}$$

For this to integrable, the coordinates $\boldsymbol{q'}$ need to be transformed such that $\epsilon'_{q'}$ can be expressed as the square absolute value of a vector. To this end, $\boldsymbol{q''}$ is defined

$$\boldsymbol{q''} = \begin{pmatrix} q'_x \\ q'_y \\ \sqrt{\alpha}q'_z \end{pmatrix}. \tag{6.37}$$

Rewriting the integral in terms of this variable achieves the desired expression for ϵ'. Moreover, it leaves a factor $1/\sqrt{\alpha}$ before the integral, the result is

$$\Pi(\boldsymbol{q}, \omega) \simeq -\frac{2}{\sqrt{\alpha}} \int \frac{d\boldsymbol{q''}}{(2\pi)^3} \left(\frac{\hbar}{m\omega}\right)^2 (q''_x q_x + q''_y q_y + \sqrt{\alpha}q''_z q_z)^2 \frac{\partial N(\epsilon)}{\partial \epsilon}\bigg|_{\epsilon=\epsilon'_{q''}}. \tag{6.38}$$

Then rescale the z-component of $\boldsymbol{q}$ to simplify the integrand, thus defining

$$\boldsymbol{q_2} = \begin{pmatrix} q_x \\ q_y \\ \sqrt{\alpha}q_z \end{pmatrix}. \tag{6.39}$$

This leaves the following expression for Π as a function of $\boldsymbol{q}_2$

$$\Pi(\boldsymbol{q}_2, \omega) \simeq -\frac{2}{\sqrt{\alpha}} \int \frac{d\boldsymbol{q}''}{(2\pi)^3} \left(\frac{\hbar}{m\omega}\right)^2 (\boldsymbol{q}'' \cdot \boldsymbol{q}_2)^2 \left.\frac{\partial N(\epsilon)}{\partial \epsilon}\right|_{\epsilon = \epsilon'_{q''}}. \tag{6.40}$$

Now the delta function can be substituted and the integration can be done in spherical coordinates, giving

$$\Pi(\boldsymbol{q}_2, \omega) \simeq \frac{2q_2^2}{(2\pi)^2 \sqrt{\alpha}} \left(\frac{\hbar}{m\omega}\right)^2 \int dq'' q''^4 \int_0^\pi d\theta \sin\theta \cos^2\theta \delta(\mu - \frac{\hbar^2 q''^2}{2m}). \tag{6.41}$$

The integral over θ results in $2/3$, while for the integral over q'' a bit more work is needed. First, substitute $u = q''$ and factor out $\hbar^2/2m$ from the delta function. The integral over q'' is then written as

$$\frac{m}{\hbar^2} \int_0^\infty du\, u^{3/2} \delta\left(\frac{2m\mu}{\hbar^2} - u\right) = \frac{m}{2\hbar^2} \left(\frac{2m\mu}{\hbar^2}\right)^{3/2}. \tag{6.42}$$

Then putting these results together and transforming back to $\boldsymbol{q}$ gives

$$\Pi(\boldsymbol{q}, \omega) = \frac{\sqrt{2}}{3\pi^2 \sqrt{\alpha}} \frac{\sqrt{m}\mu^{3/2}}{\hbar^3 \omega^2} (q_x^2 + q_y^2 + \alpha q_z^2). \tag{6.43}$$

This equation can be simplified further by using that the chemical potential is equal Fermi energy ϵ_F for low temperature, such that $\mu \simeq \epsilon_F = (\hbar^2/2m)(3\pi^2 n_e)^{3/2}$, resulting in

$$\Pi(\boldsymbol{q}, \omega) = \frac{n_e}{2\sqrt{\alpha} m \omega^2} (q_x^2 + q_y^2 + \alpha q_z^2). \tag{6.44}$$

This result is different from the derivation in UQF for the isotropic case. Note that the whole response function is divided by $\sqrt{\alpha}$ and that the z-component of the momentum is multiplied by α. Now we extrapolate the results from the electron-gas computation to the holographic density-density response function, such that it includes the p^2 term. This results in the following response function

$$\Pi'(\omega, q, p) = \frac{\left(\frac{q^2}{\sqrt{\alpha}} + \sqrt{\alpha} p^2\right) \left(\omega \mathcal{D} + i v_s^2 D_d \chi \left(\frac{q^2}{\sqrt{\alpha}} + \sqrt{\alpha} p^2\right)\right)}{\omega^3 + i\omega^2 \left(\frac{q^2}{\sqrt{\alpha}} + \sqrt{\alpha} p^2\right)(2D_s + D_d) - \omega \left(\frac{q^2}{\sqrt{\alpha}} + \sqrt{\alpha} p^2\right) v_s^2 - i v_s^2 D_d \left(\frac{q^2}{\sqrt{\alpha}} + \sqrt{\alpha} p^2\right)^2}. \tag{6.45}$$

The spectral function $-\text{Im}[\Pi']$ can be plotted for some α and p to give insight into the effects of these variables, which is done in Fig. 6.13. The effects seen in the figures can be supported by analysis of the response function. For example, the speed of sound is dependent on α and p, as $\omega = v_s \sqrt{\frac{(q^2 + \alpha p^2)}{\sqrt{\alpha}}}$.

The effects of Coulomb interactions can then be incorporated in the same way as in previous sections by performing the double-trace deformation. Effectively, the altered holographic response function can be substituted into the equation of the total density-density response function.

For the bilayer-crystal case the total density-density spectral function is depicted in Fig. 6.14 for $\alpha = 0.01$. At shorter wavelengths this figure closely resembles Fig. 6.2. A notable difference is the more pronounced out-of-phase mode, even surpassing the intensity of the in-phase mode for $pl = \pi$. Moreover, both modes are now gapped due to the altered response function.
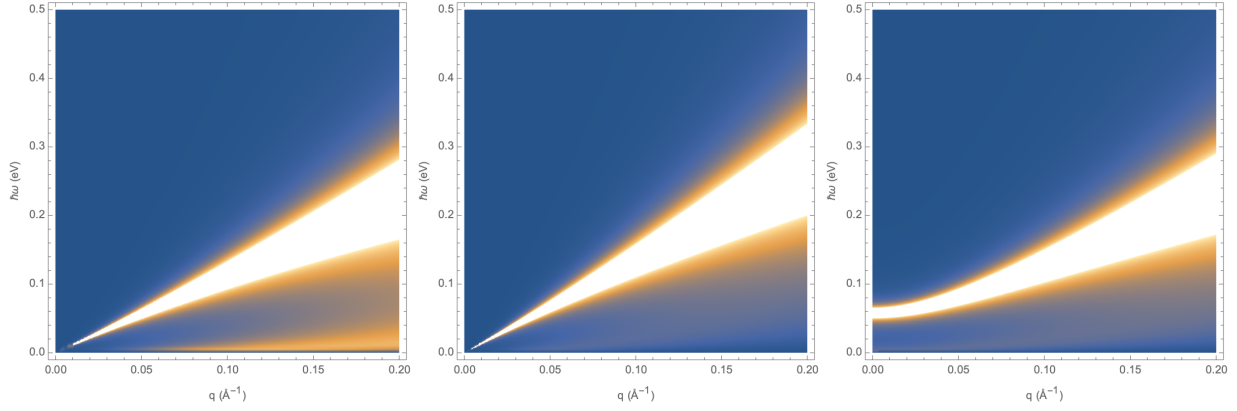
Figure 6.13: Density-density spectral function of the strong interactions modified to include hopping in the *z*-direction. The left figure is for $p = 0$, the case without hopping. This figure serves as a reference for the other two figures. In the middle figure $\alpha = 0.5$ and $p = 0$, which gives a greater speed of sound. Then finally in the right figure $\alpha = 1$ and $p = \pi/(4l)$. Note that l has no physical meaning in this context but is equal to 15.4 Å. The effect of non-zero p is that a gap forms at zero in-plane momentum.
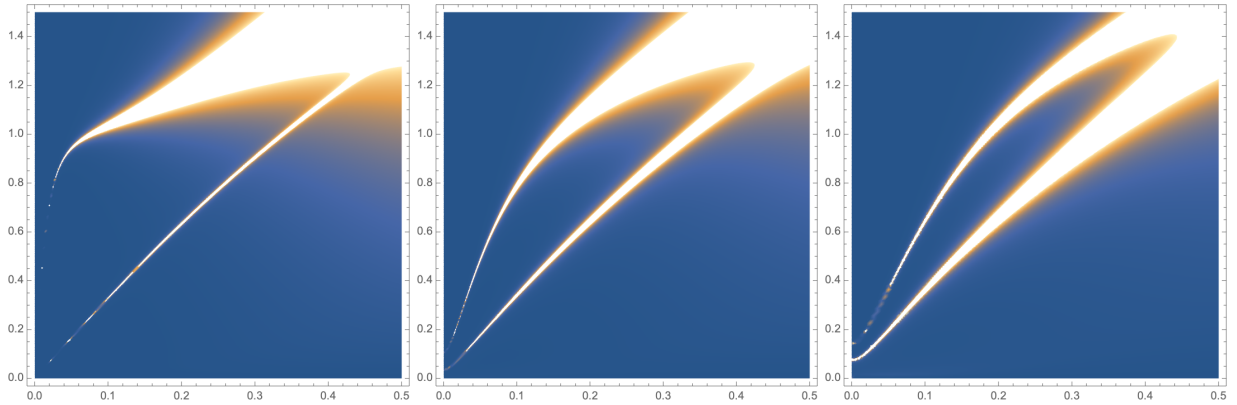
Figure 6.14: Total density-density spectral function of bilayer crystal for $\alpha = 0.01$. From left to right pl equals $\frac{\pi}{10}, \frac{\pi}{2}, \pi$. Both modes are now gapped in the middle and right figure due to the altered response function. For $pl = \frac{\pi}{10}$ it is unclear from this figure whether there is a gap at $q = 0$. But from closer inspection it follows that both modes are indeed gapped.
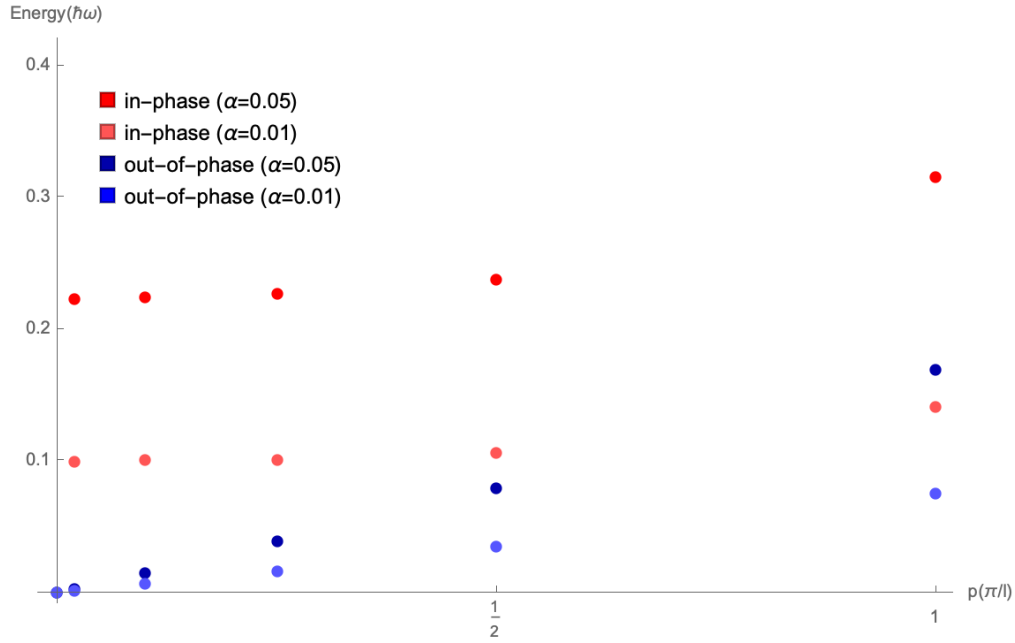
Figure 6.15: Energy of the gaps of the in-phase and out-of-phase mode of the spectral function of the bilayer crystal, at $q = 0$. The energy is plotted as function of Bloch momentum p on the x-axis. Here α characterizes the dispersion in the z-direction as in Eq. (6.45). The in-phase mode displays quadratic behaviour and the out-of-phase mode shows a linear trend. The energy gap at $p = 0$ for the in-phase mode still remains 1.0 eV as in previous sections.

To gain more insight into the effect of the added dispersion in the z-direction, the energy gap is plotted as a function of Bloch momentum p in Fig. 6.14. The in-phase mode is still gapped at 1.0 eV for $p = 0$, but now the in-phase mode is also gapped for non-zero p. From Fig. 6.14 it is clear that the size of the gap is dependent on α as well. Larger α corresponds to larger energy gap. Furthermore, the out-of-phase mode is now gapped as well, except for $p = 0$. Then for non-zero p an energy gap arises in a linear fashion in the spectral function. Likewise for the in-phase mode, a larger α means that the energy gap increases as well.

We can most easily derive the dispersion of these modes by substituting $T = 0$ into Eq. (6.45)

$$\Pi'(\omega, q, p) = \frac{(\frac{q^2}{\sqrt{\alpha}} + \sqrt{\alpha}p^2)\mathcal{D}}{\omega^2 - v_s^2(\frac{q^2}{\sqrt{\alpha}} + \sqrt{\alpha}p^2)}. \tag{6.46}$$

To avoid a mess of an equation, define $q'^2(q,p) = \frac{q^2}{\sqrt{\alpha}} + \sqrt{\alpha}p^2$, resulting in the following dispersion

$$\omega = \sqrt{\frac{e^2\mathcal{D}q'^2}{2\epsilon q}\frac{\sinh ql \pm |\sinh q(l-a) + e^{ipl}\sinh qa|}{\cosh ql - \cos pl} + v_s^2 q'^2}. \tag{6.47}$$

We use this equation to derive an expression for the energy gaps by taking the limit $q \to 0$ for $p \in (0, \pi/l]$, to obtain

$$\omega = \sqrt{\sqrt{\alpha}v_s^2 p^2 + \sqrt{\alpha}p^2\frac{e^2\mathcal{D}}{2\epsilon}\frac{l \pm |l + a(e^{ipl} - 1)|}{1 - \cos pl}}, \tag{6.48}$$

with the plus and minus sign corresponding to the in-phase and out-of-phase mode, respectively.

6.2 Derivation of parameters

A crucial part of solving the holographic puzzle is determining the unknown prefactor N_G of the gravitational action, since this allows us to make the desired quantitative predictions. First, we delve into how N_G can be determined using the plasma frequency. This computation is necessary to compare with experimental data. The following derivation holds only for the bilayer-crystal system, since the plasma frequency is used to fix certain constants. Although upon correctly accounting for a different three-dimensional structure, take for example a single-layer crystal, this derivation still holds.

Now, the values of the various constants in Eq. (4.6), the Gubser-Rocha response function, are derived. The starting point of this calculation is the thermodynamic equation of state for the electron density inside each layer obtained from the holographic dictionary as [37]

$$n = \frac{N_G'}{\sqrt{3}} \left(\frac{\mu}{\hbar v_F} \right)^2 \sqrt{1 + \frac{1}{3} \left(\frac{k_B T}{\mu} \right)^2}, \tag{6.49}$$

where $N_G' = N_G/\tilde{e}$ and $\tilde{e}$ is the dimensionless charge. Then rewrite this such that a formula for the chemical potential μ in terms of the temperature T and the electron density n is obtained, which results in

$$\mu = \sqrt{\frac{\sqrt{(k_B T)^4 + 108 \left(\frac{\hbar v_F \sqrt{n}}{\sqrt{N_G'}} \right)^4} - (k_B T)^2}{6}}. \tag{6.50}$$

Then expand this near zero temperature to obtain

$$\mu = \frac{3^{1/4} \hbar v_F \sqrt{n}}{\sqrt{N_G'}} - \frac{\sqrt{N_G'}}{4 \times 3^{5/4}} \frac{(k_B T)^2}{\hbar v_F \sqrt{n}} + \mathcal{O}(T^4). \tag{6.51}$$

Following the derivation of Mauri and Stoof [37], the result for the Drude weight of the Gubser-Rocha theory as $\mathcal{D} = N_G' \mu(n, T)/\sqrt{3}\hbar^2$ is used. Now, the relation between the Drude weight and the plasma frequency is utilised to relate N_G' to the plasma frequency. Previously, an expression for the Drude weight in a bilayer crystal was obtained in Eq. 6.10, given by

$$\mathcal{D} = \omega_{pl}^2 \frac{l\epsilon}{2e^2}. \tag{6.52}$$

The plasma frequency is essentially temperature independent [37], so it follows that the Drude weight is temperature independent, since the other quantities in Eq. (6.52) are as well. Making use of this observation the expansion for N_G' up to second order in temperature is derived with the result that

$$N_G' = \left(\frac{3^{1/4}\hbar}{v_F \sqrt{n}} \frac{\omega_{pl}^2 l\epsilon}{2e^2} \right)^2 + \frac{1}{2 \times 3^{3/2}} \left(\frac{3^{1/4}\hbar}{v_F \sqrt{n}} \frac{\omega_{pl}^2 l\epsilon}{2e^2} \right)^4 \times \left(\frac{k_B T}{\hbar v_F \sqrt{n}} \right)^2 + \mathcal{O}(T^4). \tag{6.53}$$

This expression is then used to derive all quantities in the holographic response function. Each extensive parameter is multiplied by N_G' due to the fact that is the prefactor of the action. Furthermore, the density n should be divided by N_G', since it is obtained from the square of the chemical potential.

The Drude weight is already calculated and can now be used to derive the hydrodynamic compressibility χ via a relation obtained previously [37]. Up to lowest order in temperature $\chi = \mathcal{D}/v_s^2$. While at quadratic order in temperature the difference is given by

$$\chi - \frac{\mathcal{D}}{v_s^2} = 5.12(N_G')^{3/2} \left(\frac{k_B T}{\hbar v_F \sqrt{n}} \right)^2 \frac{\sqrt{n}}{\hbar v_F}. \tag{6.54}$$

The factor $(N_G')^{3/2}$ is due to the fact that the extensive parameters χ and $\mathcal{D}$ are multiplied by N_G' and the density should be divided by N_G'.

Then the two diffusion coefficients are left, they characterize the charge diffusion and the sound diffusion. These parameters are inversely proportional to the density n, which means they should be multiplied by N_G' and are thus equal to [37]

$$D_s = \frac{1}{6\sqrt{3}} N_G' \frac{k_B T}{\hbar n}, \tag{6.55}$$

$$D_d = \frac{4\pi}{\sqrt{3}} N_G' \frac{k_B T}{\hbar n}. \tag{6.56}$$

These expressions conclude the calculation of the parameters in the holographic response function. Then to compute spectral functions and other quantities a few more material parameters are needed. For Bi-2212 that is of special interest to us here, the following material parameters are used: $\hbar\omega_{pl} = 1.0$ eV, $l = 15.4$ Å, $a = 3.2$ Å, $\epsilon/e^2 = 4.5 \times 55.263 \times 10^{-4} \text{eV}^{-1}\text{Å}^{-1}$, $v_F = 2.28 \times 10^5$ m s^{-1}, $v_s = 1.73 \times 10^5$ m s^{-1}, and $n = 6.25 \times 10^{18}$ m^{-2}. These values are used to plot the Bi-2212 density-density spectral functions and loss functions. Note that in particular $N_G' \simeq 0.45$ at zero temperature.

6.3   Single-layer crystal

Until now the layered structure has been bilayered, which means that there are two periodicities. Now, we remove one periodicity by taking the limit $a \to l/2$, such that the bilayer model reduces to a layered crystal with all neighboring layers having an equal distance $l/2$ between them. There is also a bismuth-based cuprate which has this structure, given by $Bi_2Sr_2CuO_{6+x}$, also known as Bi-2201. The response function of this crystal has been computed before [36]. In that case the intralayer physics was different, and did not represent a strange metal, but the long-range Coulomb force is treated in the same way. We show now that our response function reduces to this case of a single layer per unit cell in the limit $a \to l/2$. This is to corroborate the expression for the crystal of bilayers. From Eq. (6.8) we can deduce the following
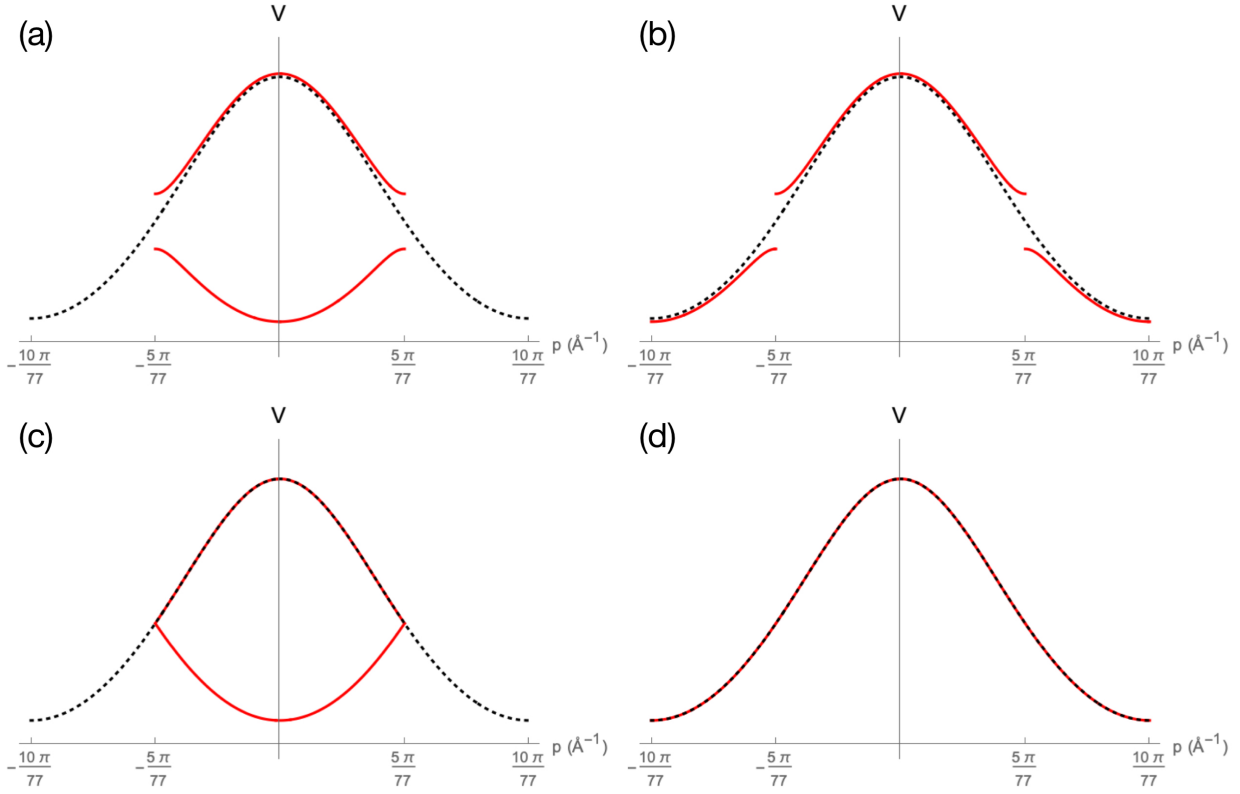
$$det\chi_{IJ}^{-1} = \left(\Pi^{-1} \right)^2 - 2\Pi^{-1}V_{11} + V_{11}^2 - V_{12}V_{21}, \tag{6.57}$$

where we have absorbed the e^2/ϵ into the potential matrix for simplicity. Then we set out to find the roots of this equation, since this determines the dispersion, by solving the quadratic formula for Π^{-1}, giving us

$$\Pi^{-1} = \frac{2V_{11} \pm \sqrt{4V_{11}^2 - 4(V_{11}^2 - V_{12}V_{21})}}{2} \tag{6.58}$$

$$= V_{11} \pm \sqrt{V_{12}V_{21}}. \tag{6.59}$$

Figure 6.16: The quantity $V_\pm$ in red is compared with $V_{\text{singlelayer}}$ in dotted black for a fixed value of $q = 0.3\ \text{Å}^{-1}$ and as a function of the Bloch momentum p. The two upper figures are plotted with value $a = 0.45l$, the two bottom figures for $a = l/2$. The minus sign of $V_\pm$ corresponds to the out-of-phase mode with a lower value and the plus sign to the in-phase mode with the higher value. In (a) and (c), we have plotted the bilayer potential for $p \in [-\pi/l, \pi/l]$ and then in (b) and (d) we have periodically extended the minus sign solution to $[-2\pi/l, -\pi/l] \cup [\pi/l, 2\pi/l]$. In this plot $l = 15.4\ \text{Å}$.

Thus telling us that the only relevant quantity related to the Coulomb-potential matrix in the dispersion is $V_\pm \equiv V_{11} \pm \sqrt{V_{12}V_{21}}$. This can be compared to the same quantity of a crystal of single layers given by [36]

$$V_{\text{singlelayer}} = \frac{\sinh\frac{ql}{2}}{2q(\cosh\frac{ql}{2} - \cos\frac{pl}{2})}, \tag{6.60}$$

with the distance between the layers taken equal to $l/2$. Note that we exclude the factor e^2/ϵ again, for sake of clarity. The corresponding expression for the bilayer case is

$$V_\pm = \frac{\sinh ql \pm |\sinh q(l-a) + e^{ipl}\sinh qa|}{2q(\cosh ql - \cos pl)}. \tag{6.61}$$

Here a is the distance between the layers in the unit cell and l is the distance between the unit cells. We plot in Fig. 6.16 $V_\pm$ for a fixed value of l and change the value of a, then we compare this with the single-layer result.

In Fig. 6.16(a) and 6.16(b) we have chosen $a = 0.45l$, which means that the two layers in the unit cell are relatively far apart and the system approaches the limit of a crystal of equidistant layers. In
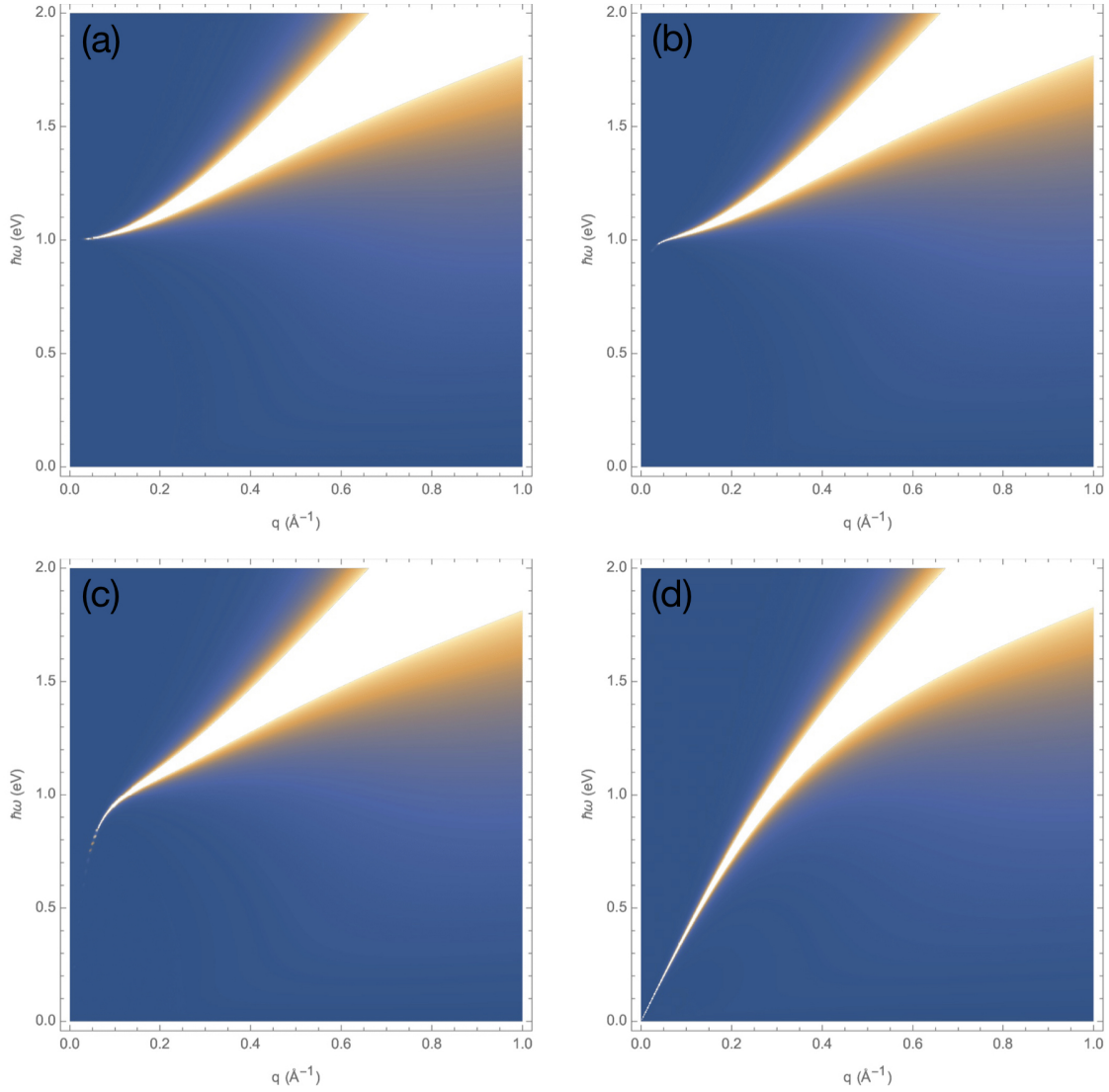
Figure 6.17: Density-density spectral function of a crystal of single layers. The distance between layers $l/2 = 7.7$ Å. In (a), $pl = 0$, there is a gapped plasmon mode. In (b)-(d), pl is $\pi/50$, $\pi/10$ and π, respectively. Here is an acoustic plasmon mode visible at long wavelengths, as in the crystal of bilayers. The temperature is fixed at room temperature $T = 293$ K.

Fig. 6.16(a) we have plotted both quantities $V_{\pm}$ for $p \in [-\pi/l, \pi/l]$. Then in Fig. 6.16(b) we have extended V_- to $[-2\pi/l, -\pi/l] \cup [\pi/l, 2\pi/l]$. This is to show that $V_{\pm}$ is already almost equal to the single-layer result in the extended-zone scheme. Then in Fig. 6.16(c) we have plotted the limiting case of $a = l/2$. We see that at $p = \pm\pi/l$ the two solutions are exactly matched to each other. Finally, in Fig. 6.16(d) we extend the minus sign solution and see that $V_{\pm}$ is equal to the single-layer potential for $l/2$, as expected. This means that in the limit $a \to l/2$ the crystal of bilayers reduces to the crystal of single layers. Which reinforces that the expression for the bilayer Coulomb potential matrix is correct.

Moving forward, we evaluate the density-density spectral function of the crystal of single layers in

Fig. 6.17. Comparing these figures with previous work [36], we see that this spectral function also has a gapped mode for $p = 0$. The plasma frequency is the same, $\hbar\omega_{pl} = 1.0$ eV. This is because the three-dimensional density of electrons has not changed, since there still is one layer per $l/2$ in the z-direction. And that is what determines the plasma frequency. Mathematically the reason is that $2n/l = n/(l/2)$. In the other subplots the behavior is as expected, it is similar to the in-phase mode of Fig. 6.1. For $pl/2 = \pi/50$, the mode approaches 1.0 eV but then quickly goes to zero as $q \to 0$. For increasing p the mode becomes less steep for small q until for $pl/2 = \pi$ the lowest speed of sound is reached. In the limit $T \to 0$ we can again derive the dispersion relation

$$\omega = \sqrt{\frac{e^2 \mathcal{D} q}{2\epsilon} \frac{\sinh\left(\frac{ql}{2}\right)}{\cosh\left(\frac{ql}{2}\right) - \cos\left(\frac{pl}{2}\right)} + v_s^2 q^2}. \tag{6.62}$$

The plasma frequency is exactly the same as in the two-layer case, since the three-dimensional density is kept constant. So the dispersion relation becomes

$$\omega = \sqrt{\omega_{pl}^2 \frac{ql'}{2} \frac{\sinh\left(ql'\right)}{\cosh\left(ql'\right) - \cos\left(pl'\right)} + v_s^2 q^2}, \tag{6.63}$$

where $l' = l/2$ is the distance between the layers. The plasma frequency is given by $\omega_{pl} = \sqrt{e^2 \mathcal{D}/l'\epsilon}$. Using this equation we can derive the renormalized speed of sound

$$v(p) = \sqrt{v_s^2 + \omega_{pl}^2 \frac{l'^2/2}{1 - \cos\left(pl'\right)}}, \tag{6.64}$$

confirming that $pl/2 = pl' = \pi$ gives the lowest speed of sound. The above equation is not valid exactly for $p = 0$, of course. Besides the plasmon mode, this spectral function also contains a diffusive mode. Although this mode is not visible due its low intensity compared to the plasmon mode. Finally, we wish to emphasize that the spectral function in Fig. 6.17 is in accordance with a number of resonant inelastic X-ray scattering (RIXS) studies on the strange-metal phase of cuprates with one CuO_2 layer per unit cell. In two of these RIXS studies on the electron-doped cuprate $La_{2-y}Ce_yCuO_{4+x}$ (LCCO) [48] and the hole-doped cuprates $La_{2-y}Sr_yCuO_{4+x}$ (LSCO) and $Bi_2Sr_{1.6}La_{0.4}CuO_{6+x}$ (Bi-2201) [16], an acoustic plasmon dispersion is measured. The corresponding RIXS intensity maps are qualitatively similar to Fig. 6.17, with the corresponding non-zero values of pl'. The density-density spectral function in Fig. 6.17 is calculated using an approach that is appropriate for strange metals, namely using the Gubser-Rocha model. This validates the conclusion that the acoustic branches which are measured in RIXS studies can be attributed to an acoustic plasmon.

Plasmons in other cuprates

Having thoroughly treated Bi-2212, we move on to some other cuprates and compute the density-density spectral function. This allows us to compare with more experimental data. We grasp this opportunity by directly comparing with RIXS measurements performed on the plasmon energy of the relevant cuprates. First, we treat a cuprate with bilayer-crystal structure, $YBa_2Cu_3O_{7-x}$ (YBCO). Thereafter we deal with the single-layer crystal $Bi_2Sr_2CuO_{6+x}$ (Bi-2201), which is the simpler version of the bilayer cuprate Bi-2212. In Table 7.1, we summarize the important parameters for these cuprates.

Cuprate Overview			
Cuprate	Plasma Energy ($\hbar\omega$ (eV))	Distance between layers (Bilayer) (Å)	Distance between layers (Single Layer) (Å)
Bi-2212	1.0	15.4, 3.2	-
YBCO	1.4	11.7, 2.9	-
Bi-2201	0.85	-	12.3

Table 7.1: Overview of the important parameters of the cuprates treated in this thesis. In the first column we name the cuprates, then in the second column the energy gap of the optical plasmon. The third column contains the out-of-plane distances for the bilayer-crystal cuprates, the first parameter is the distance between the pairs of layers, the second the distance between two closely-spaced layers. In the fourth column the distance between the layers in single-layer cuprates is shown.

7.1 $YBa_2Cu_3O_{7-x}$ (YBCO)

In 1987 it was announced that a cuprate was found with a T_c exceeding the temperature of liquid nitrogen, approximately 77 K. They found the the Yttrium-based $YBa_2Cu_3O_{7-x}$ (YBCO), with a critical temperature around 93 K [10]. This cuprate has a bilayer structure, similarly to Bi-2212, although the atomic structure differs significantly from Bi-2212. Take a look at the unit cell displayed in Fig. 7.1. A new phenomenon appears, namely CuO chains situated on top of the CuO_2 planes. This might complicate analysis of this cuprate, but we just assume that it is part of the charge reservoir.
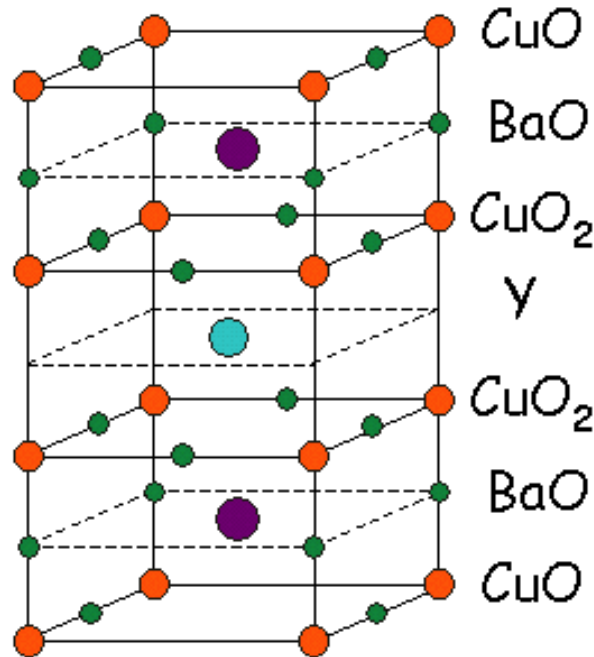
Figure 7.1: Atomic structure of the unit cell of YBCO. Source: [10].

To compute the density-density spectral function we need the values of certain parameters. Firstly, the distance between the layers is mentioned in the table at the start of this chapter. The background dielectric constant is similar to the bismuth-based cuprates at approximately $4.5\epsilon_0$ [12] and we also assume the same Fermi velocity. In-plane lattice constants are $a = 3.89$ Å, $b = 3.88$ Å. We use these parameters to go through the same process as in Section 6.2 and derive the other needed parameters. Then we perform the double-trace deformation to obtain the density-density response function.

The spectral function is displayed in Fig. 7.2, together with data points from a recent paper [19]. It is clear that the data does not fit either the in-phase or the out-of-phase mode. For small in-plane momentum the measured plasmon energy is between the two modes and as the in-plane momentum is increased the measured energy moves to the out-of-phase mode. This deviation from our predictions might be due to shortcomings of our model or there could be other causes.

It might that the measured plasmon is due to the superposition of two widened modes. To support this claim, we plot the plasmon energy for a constant in-plane momentum in Fig. 7.3. It is clear that the in-phase mode is more prominently present and therefore it is not unthinkable that upon even further widening the peak might lie somewhere between the two modes.

Another effect that could be at play is inter-layer hopping. As we have seen in Section 6.1.4, it induces a gap at zero in-plane momentum. This aligns with the the measured dispersion, which does not to seem acoustic. Furthermore, the layers of YBCO are much closer together than those of Bi-2212, thus possibly enhancing inter-layer hopping.
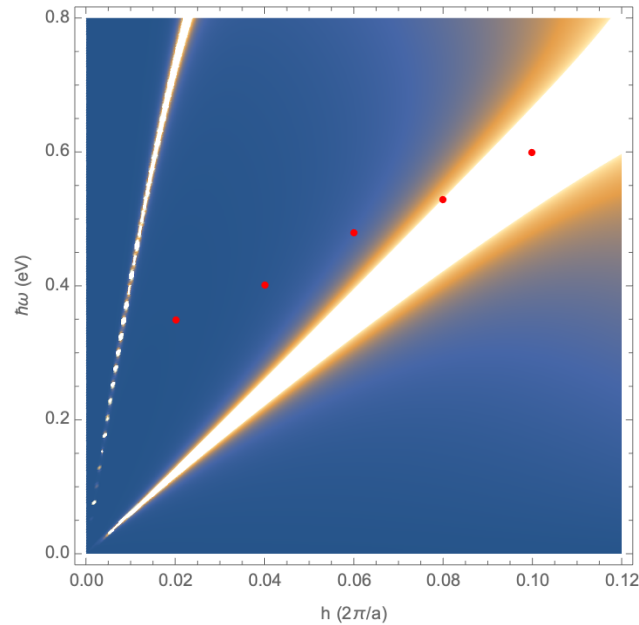
Figure 7.2: Density-density spectral function of YBCO for $pl = 0.2\frac{\pi}{l}$. The y-axis is plotted for h, the in-plane momentum, in units of $2\pi/a$, a the in-plane lattice constant. The red dots is data from Figure 3(b) of [19].
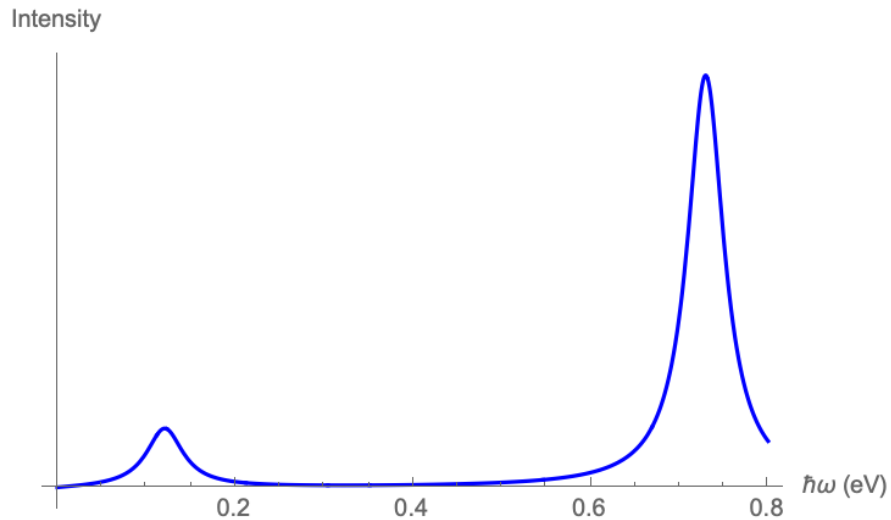
Figure 7.3: Intensity of plasmon mode for constant in-plane momentum $0.02 \times 2\pi/a$, with a the in-plane lattice unit. Widening of the modes achieved by substituting $\hbar\omega \rightarrow \hbar\omega + \frac{i}{40}$. The intensity of the in-phase mode dominates the out-of-phase mode.
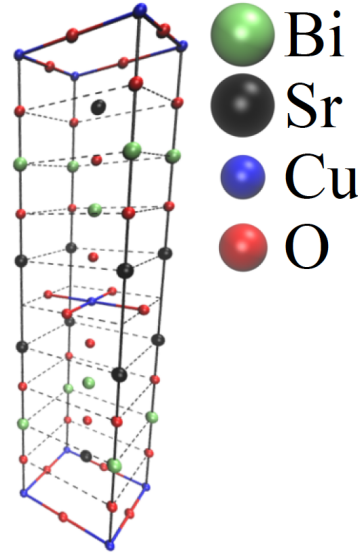
Figure 7.4: The unit cell of Bi-2201 contains three equidistant CuO_2 planes. Adjacent layers are rotated 45 degrees. Source: [26].

7.2 $Bi_2Sr_2CuO_{6+x}$ (Bi-2201)

This section is dedicated to the cuprate Bi-2201, the simpler counterpart of the cuprate Bi-2212, with a layered structure consisting of equidistant copper-oxide planes. The structure formula is $Bi_2Sr_2CuO_{6+x}$. Note that the numbers in the nomenclature of these bismuth-based cuprates refer to the structure formula. For example, there is no calcium atom in Bi-2201.

Firstly, the important parameters for this material are taken from Table 7.1, $\hbar\omega_{pl} = 0.85$ eV, $\epsilon = 4.5\epsilon_0$, $l = 12.3$ Å. Using these parameters the two-dimensional Drude weight is calculated and allows the density-density response to be computed as well by following the derivation in Section 6.2. Note that the formula for the Drude weight is now

$$\mathcal{D} = \omega_{pl}^2 \frac{l\epsilon}{e^2},\tag{7.1}$$

the factor two in the denominator has disappeared due to the single-layered nature of Bi-2201. Since the plasma frequency is a bulk property and the Drude weight here is two-dimensional, the distance between the layers is involved in the above formula. Keep in mind the formula for the plasma frequency in terms of three-dimensional Drude weight

$$\omega_{pl} = \sqrt{\frac{e^2 \mathcal{D}_{3D}}{\epsilon}},\tag{7.2}$$

this elucidates the absence of the factor of two in Eq. (7.1).

Having computed the density-density response function of the strong interactions the double-trace deformation can be applied to obtain the full density-density response function. Then the density-density spectral function can be plotted and compared with experiment, as seen in Fig. 7.5. The result is that the spectral function aligns with the dispersion measured in the experimental setup. The data is obtained from Figure 2(c) of "Detection of Acoustic Plasmons in Hole-Doped Lanthanum
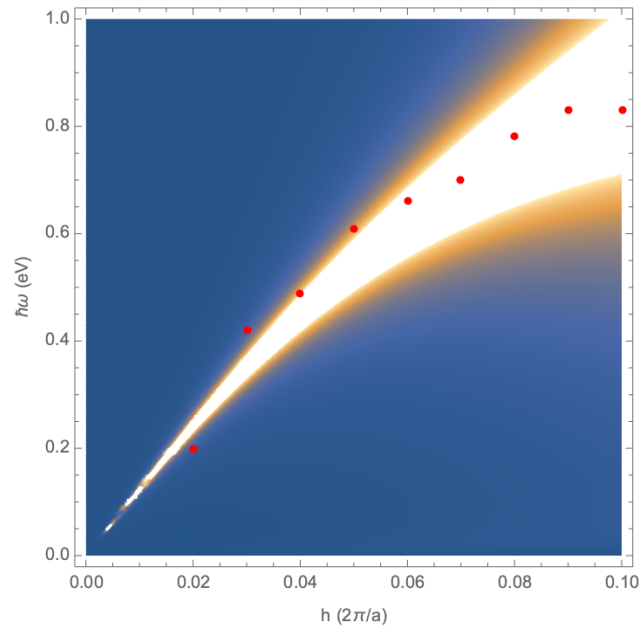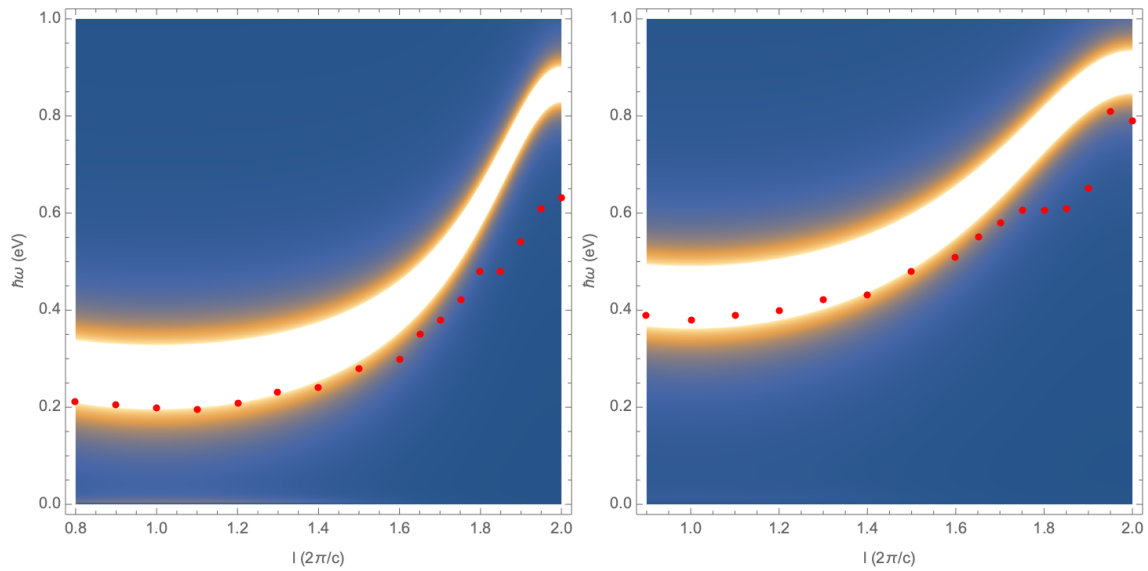
Figure 7.5: Density-density spectral function for Bi-2201 for $pl = -0.5\frac{\pi}{l}$. The y-axis is plotted for h, the in-plane momentum, in units of $2\pi/a$, a the in-plane lattice constant. The red dots is data from Figure 2(c) of "Data from Detection of Acoustic Plasmons in Hole-Doped Lanthanum and Bismuth Cuprate Superconductors Using Resonant Inelastic X-Ray Scattering" [16].

and Bismuth Cuprate Superconductors Using Resonant Inelastic X-Ray Scattering" in the form of red dots [16]. Note that the uncertainty is not shown here and is quite significant. Especially the low-momenta measurements have larger uncertainty.

Then in Fig. 7.6 another comparison is made with RIXS experiments. Only this time the out-of-plane momentum dependence is plotted. The data plotted over the spectral function generally match, except for the largest out-of-plane momentum. These measurements do have large error bars so are not the most accurate.

Figure 7.6: Density-density spectral function of Bi-2201 for $q = 0.03\,2\pi/a$ on the left side and $q = 0.05\,2\pi/a$ on the right side, as a function of out-of-plane momentum. The y-axis is plotted for I in units of $2\pi/c$, with c twice the distance between the layers. The red dots is data from Figure 2(c) of "Detection of Acoustic Plasmons in Hole-Doped Lanthanum and Bismuth Cuprate Superconductors Using Resonant Inelastic X-Ray Scattering" [16].

CHAPTER 8

Conclusion and Outlook

In this thesis we discussed a layered strange metal and computed the density-density response of this system. More specifically, we considered a cuprate with a bilayer-crystal structure, as is the case for Bi-2212. We modeled the strong short-range interactions in each CuO_2 layer using the holographic Gubser-Rocha model and we obtained the associated density-density response function for these strong interactions from the gauge/gravity duality. In addition, we incorporated the long-range Coulomb interactions by means of a double-trace deformation, which results in the density-density response function of the layered strange metal. We calculated the density-density spectral function for arbitrary values of the out-of-plane Bloch momentum p, and find both an in-phase and an out-of-phase mode. We computed the dispersion of these modes and showed that the in-phase plasmon mode is gapped for $p = 0$, while it has an acoustic nature at long wavelengths for non-zero p. The out-of-phase mode always has an acoustic nature in the long-wavelength limit and its dispersion is virtually independent of p. However, the intensity of the out-of-phase mode does depend on p, starting with vanishing intensity at $p = 0$ and gradually increasing until $p = \pi/l$.

Furthermore, we extracted the conductivity of the bilayer crystal from the density-density response function, taking into account the disorder that is present in experiments by introducing Planckian dissipation. In the parameter regime typical for cuprates there is always a Drude peak visible in the conductivity with a dc-resistivity linear in temperature. Moreover, we used the total density-density response function to construct the loss function which is measured in transmission EELS and we discuss its behavior. In principle, the loss function only contains a single peak belonging to the in-phase plasmon mode, since the intensity of the out-of-phase mode is smaller in the relevant regime of p. Only when allowing for a large experimental uncertainty in the out-of-plane momentum p, and with a transverse momentum close to zero, there are two wide peaks visible. The mode around 1.0 eV is due to the contributions close to $p = 0$, while the lower energy peak arises from contributions with a larger value of p. We also computed the effects of Umklapp scattering due to supermodulation, the incommensurate periodicity in the lattice. We displayed the results in the form of the density-density spectral function and the loss function. The main effect measured in the loss function is that Umklapp scattering lowers the energy of the peaks, with the greatest shift in the out-of-phase mode. Thereafter, we modeled hopping between the CuO_2 layers by altering the two-dimensional Gubser-Rocha response to include dispersion in the z-direction. This results in the in-phase mode retaining its gap for non-zero p, while the out-of-phase mode also obtains a gap for non-zero p.

Then in Chapter 7 we computed the density-density response for Bi-2201, which has the structure of a single-layer crystal. We obtained the spectral function of this geometry in Chapter 6 as a test for the bilayer-crystal expression, but entering the parameters typical for Bi-2201 also allows us to provide more results to compare with experimental data. And we also computed the density-density response for YBCO, which has a bilayered structure, similar to Bi-2212.

Throughout this thesis, we made a number of assumptions to simplify the system. For example, in the concrete example of Bi-2212 that we considered, there is a difference between the atomic structure in between the pair of layers close to each other and in between the pairs of layers. Therefore, the different dielectric constants might quantitatively influence the behavior of plasmons. Another assumption we made is that there is rotational invariance in each layer, which is of course not exactly the case, since there is a square lattice structure in the CuO_2 layers. Although this lattice structure does not influence the dispersion of the plasmon for small q, it does play a role for larger values of q. Hence, it would be interesting to include the lattice in the future. Besides, many cuprates are known to have an extra periodicity which modulates their atomic lattice, known as supermodulation [33, 54], which we partially treat by including Umklapp scattering caused by the periodicity. But it might also have other effects, such as charge-density waves.
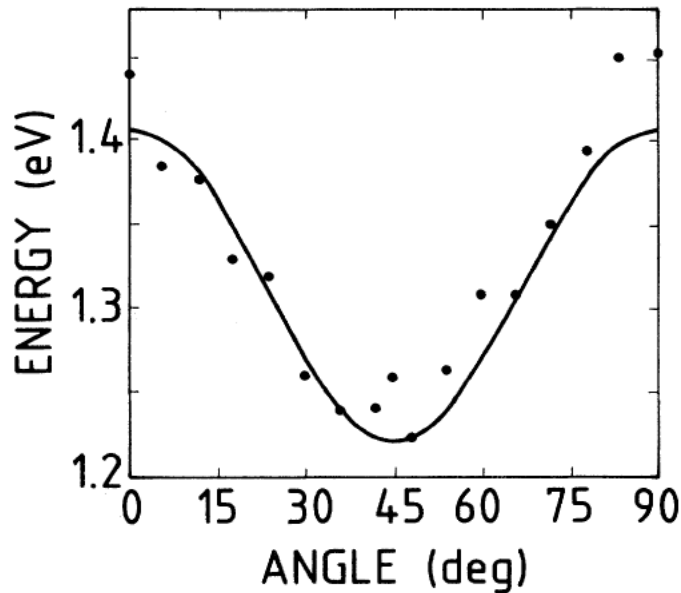
Figure 8.1: Plasmon energy measured in Bi-2212 by Nücker et al. For constant in-plane momentum $q = 0.3\,\text{Å}^{-1}$. Here, 0 degrees indicates the nodal direction of the cuprate. Source: [13].

The findings in this thesis provide new insights into the plasmons in layered strange metals. In particular, we notice that the holographic Gubser-Rocha model can reproduce the acoustic plasmon branches that have been observed in RIXS experiments on cuprates [16, 17]. Additionally, the results contain many other aspects of the strange metal measured in experiments, like the linear-in-T resistivity or the repeatedly measured optical plasmon mode. But there are definitely properties that are not incorporated in the model, take for example the anisotropic dispersion of the optical plasmon measured by Nücker et al [13]. Here, the optical plasmon was measured for in-plane momentum $q = 0.3\,\text{Å}^{-1}$, but in different in-plane directions. Their results are displayed in Fig. 8.1.

Since we assume rotational invariance our results do not display this anisotropy. Somehow this has to be incorporated correctly. Although we did consider Umklapp scattering, which breaks the rotational symmetry, it did not agree with the results found by Nücker et al. Thus indicating that another solutions needs to be found.

A possible solution might still be Umklapp scattering, but then from the lattice itself. Since this periodicity aligns with the measured periodicity of 90 degrees. A drawback is that the effect is most likely very small for long wavelengths.

A more direct approach would be to impose angular dependence on the Gubser-Rocha response, such that, for example, the speed of sound is dependent on the direction. This would require, however, robust experimental arguments to justify it.

Another possible future endeavor could be reconsidering the holographic model that describe the strong short-range interactions in the CuO_2 layers. Although the Gubser-Rocha model has been used to effectively to describe strange metals, it has also been proven that it can never describe all properties of the strange metal [31]. It might be the case that another holographic model, which does deliver all the desired properties, is needed to better understand the strange-metal phase. Unfortunately, it is not possible to set certain requirements and immediately obtain the correct holographic model, due to the nature of bottom-up computations. However, if a more suitable holographic model is found and the density-density response function can be extracted, including long-range Coulomb interactions is then achieved in the same manner as described in this thesis.

Looking back at the phase diagram of cuprates, notice that the behavior of these materials is greatly dependent on doping. It would be interesting therefore to research how plasmons are affected by doping. This could possibly help understand the strange-metal phase.

Finally, the goal of this thesis is to inspire more research into plasmons in layered strange metals, either in the form of more experiments or in the form of more theoretical analysis. Hopefully, this will improve our understanding of this mysterious phase of matter. It will be interesting to see whether the approach using holographic models leads to more answers in the future.

Acknowledgments

Henk, I really enjoyed working with you on this project. The conversations about physics and also about our favourite football club were great. I am grateful for your guidance!

Kees and *Thijs*, thanks for the warm welcome I received when I visited your offices in Eindhoven. I also enjoyed the online meetings we had during the year.

Sebastiaan, Roeland, Luuk, Lars and *Casper*, I really enjoyed the coffee and lunch breaks we shared. As well as the discussions about physics or LaTeX.

Bilayer-crystal Potential

The computation of the potential matrix of the bilayer-crystal geometry is quite long, therefore we treat it extensively in this appendix. We pick up from Eq. (6.3) and from there work out the expression to derive the potential matrix.

The starting point is thus the effective boundary action

$$
\Delta S_C = \frac{1}{2} \int \frac{d\omega d^2 q}{(2\pi)^3} \int \frac{dq_z}{2\pi} \sum_{n,m} \begin{pmatrix} J_1^\mu(-\omega, -\boldsymbol{q}, nl - a/2) \\ J_2^\mu(-\omega, -\boldsymbol{q}, nl + a/2) \end{pmatrix}
$$
$$
\cdot \eta_{\mu\nu} \frac{e^2}{\epsilon} \frac{e^{-iq_z(n-m)l}}{q^2 + q_z^2} \begin{pmatrix} 1 & e^{-iq_z a} \\ e^{iq_z a} & 1 \end{pmatrix} \cdot \begin{pmatrix} J_1^\nu(\omega, \boldsymbol{q}, ml - a/2) \\ J_2^\nu(\omega, \boldsymbol{q}, ml + a/2) \end{pmatrix}.
$$

(A.1)

This equation is the bilayer-crystal equivalent of Eq. (5.4). Although we now have to deal with two summations and a more complicated integrand, we can actually first perform the integration over q_z,

$$
\int \frac{dq_z}{2\pi} \frac{e^{-iq_z(n-m)l \pm iq_z a}}{q^2 + q_z^2} = \frac{e^{-q|nl - ml \mp a|}}{2q},
$$

(A.2)

and substitute into the boundary action, to obtain

$$
\Delta S_C = \frac{1}{2} \int \frac{d\omega d^2 q}{(2\pi)^3} \sum_{n,m} \begin{pmatrix} J_1^\mu(-\omega, -\boldsymbol{q}, nl - a/2) \\ J_2^\mu(-\omega, -\boldsymbol{q}, nl + a/2) \end{pmatrix}
$$
$$
\cdot \eta_{\mu\nu} \frac{e^2}{2\epsilon q} \begin{pmatrix} e^{-q|n-m|l} & e^{-q|nl - ml + a|} \\ e^{-q|nl - ml - a|} & e^{-q|n-m|l} \end{pmatrix} \cdot \begin{pmatrix} J_1^\nu(\omega, \boldsymbol{q}, ml - a/2) \\ J_2^\nu(\omega, \boldsymbol{q}, ml + a/2) \end{pmatrix}.
$$

(A.3)

The next task is performing the summation over n and m, but we first need to rewrite the current such that it does not contain the layer indices. To this end, we Fourier transform the periodicity of the current over n and m to the Bloch momentum p, i.e.,

$$
J_1^\mu(\omega, \boldsymbol{q}, nl - a/2) = (l/2\pi) \int_{-\pi/l}^{\pi/l} dp J_1^\mu(\omega, \boldsymbol{q}, p) e^{ip(nl - a/2)}.
$$

(A.4)

The Bloch momentum is in the direction perpendicular to the layers, since the periodicity is in n and m. Inserting the corresponding Fourier transform gives

$$\Delta S_C = \frac{1}{2} \int \frac{d\omega d^2q}{(2\pi)^3} \int_{-\pi/l}^{\pi/l} \frac{ldp}{2\pi} \int_{-\pi/l}^{\pi/l} \frac{ldp'}{2\pi} \sum_{n,m} \begin{pmatrix} J_1^\mu(-\omega,-\boldsymbol{q},p)e^{ip(nl-a/2)} \\ J_2^\mu(-\omega,-\boldsymbol{q},p)e^{ip(nl+a/2)} \end{pmatrix}$$
$$\cdot \eta_{\mu\nu} \frac{e^2}{2\epsilon q} \begin{pmatrix} e^{-q|n-m|l} & e^{-q|nl-ml+a|} \\ e^{-q|nl-ml-a|} & e^{-q|n-m|l} \end{pmatrix} \begin{pmatrix} J_1^\nu(\omega,\boldsymbol{q},p')e^{ip'(ml-a/2)} \\ J_2^\nu(\omega,\boldsymbol{q},p')e^{ip'(ml+a/2)} \end{pmatrix}. \quad (A.5)$$

The exponents can then be distributed to the corresponding matrix components, after which we start with analyzing the sum over n and m. We take the bottom left component as example and work it out,

$$\sum_{n,m} e^{-q|(n-m)l-a|+ip(nl+a/2)+ip'(ml-a/2)}$$

$$= e^{-i(p'-p)a/2} \sum_m e^{imlp'} \left(\sum_{n<m} e^{q((n-m)l-a)+ipnl} + e^{-qa+ipml} + \sum_{n>m} e^{-q((n-m)l-a)+ipnl} \right)$$

$$= e^{-i(p'-p)a/2} (e^{-qa} \sum_m e^{imlp'-mlq} \sum_{n<m} e^{qnl+ipnl} + \sum_m e^{-qa+iml(p'+p)} + e^{qa} \sum_m e^{imlp'+mlq} \sum_{n>m} e^{-qnl+ipnl})$$

$$= e^{-i(p'-p)a/2} (e^{-qa} \sum_m e^{iml(p'+p)} \sum_{n<0} e^{qnl+ipnl} + \sum_m e^{-qa+iml(p'+p)} + e^{qa} \sum_m e^{iml(p'+p)} \sum_{n>0} e^{-qnl+ipnl})$$

$$= e^{-i(p'-p)a/2} \sum_m e^{iml(p+p')} \left(e^{-qa} \sum_{n<0} e^{qnl+ipnl} + e^{-qa} + e^{qa} \sum_{n>0} e^{-qnl+ipnl} \right). \quad (A.6)$$

In the first step the term independent of n and m is taken to the front and the absolute value is worked out. Then we put all terms independent of n before the sum over n. In the third step m is factored out such that the sum is either for $n < 0$ or $n > 0$ and there appears a common factor before the sums over n. Recognize that the sum over m is a delta function and substitute it,

$$= e^{-i(p'-p)a/2} \sum_m e^{iml(p+p')} \left(e^{-qa} \sum_{n<0} e^{qnl+ipnl} + e^{-qa} + e^{qa} \sum_{n>0} e^{-qnl+ipnl} \right)$$

$$= \frac{2\pi}{l} \delta(p+p') \left(\sum_{n>0} (e^{-nlq-inlp-qa} + e^{-nlq+inlp+qa}) + e^{-qa} \right) e^{-i(p'-p)a/2}$$

$$= \frac{2\pi}{l} \delta(p+p') \left(\sum_{n=0}^\infty e^{-nlq-inlp-qa} + \sum_{n=1}^\infty e^{-nlq+inlp+qa} \right) e^{-i(p'-p)a/2} \quad (A.7)$$

$$= \frac{2\pi}{l} \delta(p+p') \left(\frac{e^{-qa}}{1-e^{-ipl-ql}} + \frac{e^{-q(l-a)+ipl}}{1-e^{ipl-ql}} \right) e^{-i(p'-p)a/2}.$$

In the first step the sum over negative n is inverted, thereafter e^{qa} is absorbed into the first sum, such that now it also sums over $n = 0$. Then, recognize the geometric series and substitute both expressions. These two separate fractions can be combined by rewriting them such that they obtain the same denominator, resulting in

$$\frac{2\pi}{l} \delta(p+p') \left(\frac{\sinh(l-a)q + e^{ipl} \sinh qa}{\cosh ql - \cos pl} \right) e^{-i(p'-p)a/2}. \quad (A.8)$$

After substituting Eq. (A.8) and the other matrix components and subsequently integrating over p' the following result is obtained

$$\Delta S_C = \frac{1}{2} \int \frac{d\omega d^2 q}{(2\pi)^3} \int_{-\pi/l}^{\pi/l} \frac{l dp}{2\pi} \begin{pmatrix} J_1^\mu(-\omega, -\boldsymbol{q}, -p) \\ J_2^\mu(-\omega, -\boldsymbol{q}, -p) \end{pmatrix} \cdot \frac{e^2 \eta_{\mu\nu}}{\epsilon} V(q, p) \cdot \begin{pmatrix} J_1^\nu(\omega, \boldsymbol{q}, p) \\ J_2^\nu(\omega, \boldsymbol{q}, p) \end{pmatrix}, \qquad \text{(A.9)}$$

with the following expression for the 2×2 matrix V, with the same form as for a bilayered electron-gas [49, 50],

$$V(q, p) = \frac{1}{2q(\cosh ql - \cos pl)} \begin{pmatrix} \sinh ql & (\sinh q(l-a) + e^{-ipl} \sinh qa)e^{-ipa} \\ (\sinh q(l-a) + e^{ipl} \sinh qa)e^{ipa} & \sinh ql \end{pmatrix}.$$

$$\text{(A.10)}$$

Bibliography

[1] R.A. Cooper and et al. Anomalous criticality in the electrical resistivity of $la_{2-x}sr_xcuo_4$. *Science*, 323:603, 2009.

[2] J.A.N. Bruin, H. Sakai, R.S. Perry, and A.P. Mackenzie. Similarity of scattering rates in metals showing t-linear resistivity. *Science*, 339:804, 2013.

[3] C. Proust and L. Taillefer. The remarkable underlying ground states of cuprate superconductors. *Annu. Rev. Condens. Matter Phys.*, 10:409, 2019.

[4] N.E. Hussey, K. Takenaka, and H. Takagi. Universality of the mott–ioffe–regel limit in metals. *Philos. Mag.*, 84:27 2847–2864, 2004.

[5] P.W. Anderson. *The Theory Of Superconductivity In The High-Tc Cuprate Superconductors*. Princeton Univ. Press, 1997.

[6] N. Plakida. *High-temperature Cuprate Superconductors*. Springer, 2010.

[7] J. Bardeen, L. N. Cooper, and J. R. Schrieffer. Theory of superconductivity. *Phys. Rev.*, 108:1175–1204, Dec 1957.

[8] W. L. McMillan. Transition temperature of strong-coupled superconductors. *Phys. Rev.*, 167:331–344, Mar 1968.

[9] A. Schilling, M. Cantoni, J.D. Guo, and H.R. Ott. Superconductivity above 130 k in the hg–ba–ca–cu–o system. *Nature*, 363:56–58, 1993.

[10] https://hoffman.physics.harvard.edu/materials/SCintro.php.

[11] N. Nücker, H. Romberg, S. Nakai, and et al. Plasmons and interband transitions in $bi_2sr_2cacu_2o_8$. *Phys. Rev. B.*, 39:12379(R), 1989.

[12] I. Bozovic. Plasmons in cuprate superconductors. *Phys. Rev. B.*, 42:4, 1990.

[13] N. Nücker, U. Eckern, J. Fink, and P. Müller. Long-wavelength collective excitations of charge carriers in high-tc superconductors. *Phys. Rev. B.*, 44:7155(R), 1991.

[14] J. Levallois and et al. Temperature-dependent ellipsometry measurements of partial coulomb energy in superconducting cuprates. *Phys. Rev. X.*, 6:031027, 2016.

[15] M Mitrano and et al. Anomalous density fluctuations in a strange metal. *Proc. Natl. Acad. Sci.*, 115:21, 2018.

[16] A. Nag and et al. Detection of acoustic plasmons in hole-doped lanthanum and bismuth cuprate superconductors using resonant inelastic x-ray scattering. *Phys. Rev. Lett.*, 125:257002, 2020.

[17] M. Hepting and et al. Gapped collective charge excitations and interlayer hopping in cuprate superconductors. *Phys. Rev. Lett.*, 129:047001, 2022.

[18] M. Hepting and et al. Evolution of plasmon excitations across the phase diagram of the cuprate superconductor $la_{2-x}sr_xcuo_4$. *Phys. Rev. B.*, 107:214516, 2023.

[19] M. Bejas and et al. Plasmon dispersion in bilayer cuprate superconductors, 2023.

[20] J. Maldacena. The large n-limit of superconformal field theories and supergravity. *Int. J. Theor. Phys.*, 38:1113–1133, 1999.

[21] S.A Hartnoll, A. Lucas, and S. Sachdev. *Holographic Quantum Matter*. 2016.

[22] S.S. Gubser and F.D. Rocha. Peculiar properties of a charged dilatonic black hole in ads_5. *Phys. Rev. D.*, 81:046001, 2010.

[23] S. Smit and et al. Momentum-dependent scaling exponents of nodal self-energies measured in strange metal cuprates and modelled using semi-holography, 2021.

[24] E. Witten. Multi-trace operators, boundary conditions, and ads/cft correspondence. 2002.

[25] W. Mück. An improved correspondence formula for ads/cft with multi-trace operators. *Phys. Lett. B*, 531:301–304, 2002.

[26] T.J.N van Stralen. Probing charge density oscillations in the cuprate superconductor bi-2212 using electron energy loss spectroscopy, 2023.

[27] Gabriele F. Giuliani and Giovanni Vignale. *Quantum Theory of the Electron Liquid*. Cambridge University Press, Cambridge, UK, 2005.

[28] H.T.C. Stoof, K.B. Gubbels, and D. Dickerscheid. *Ultracold quantum fields*. Springer, 2009.

[29] M. Blake and A. Donos. Quantum critical transport and the hall angle in holographic models. *Phys. Rev. Lett.*, 114:021601, 2015.

[30] A. Amoretti, M. Baggioli, N. Magnoli, and D. Musso. Chasing the cuprates with dilatonic dyons. *J. High Energ. Phys.*, 2016:113, 2016.

[31] Y. Ahn, M. Baggioli, H. Jeong, and K. Kim. Holographic gubser-rocha model does not capture all the transport anomalies of strange metals. 2023. https://doi.org/10.48550/arXiv.2307.04433.

[32] B. Keimer, S.A. Kivelson, M.R. Norman, S. Uchida, and J. Zaanen. From quantum matter to high-temperature superconductivity in copper oxides. *Nature*, 518:179–186, 2015.

[33] C. C. Tsuei and J. R. Kirtley. Pairing symmetry in cuprate superconductors. *Rev. Mod. Phys.*, 72:969, 2000.

[34] Steven S Gubser, Igor R Klebanov, and Alexander M Polyakov. Gauge theory correlators from non-critical string theory. *Physics Letters B*, 428(1-2):105–114, 1998.

[35] Edward Witten. Anti de sitter space and holography. *arXiv preprint hep-th/9802150*, 1998.

[36] E. Mauri and H.T.C. Stoof. Screening of coulomb interactions in holography. *J. High Energ. Phys.*, 2019:35, 2019.

[37] E. Mauri and H.T.C. Stoof. Coulomb drag between two strange metals. *Phys. Rev. B.*, 106:205116, 2022.

[38] E. Witten. Anti-de sitter space and holography. *Adv. Theor. Math. Phys.*, 2:253–291, 1998.

[39] J. Zaanen and et al. *Holographic Duality In Condensed Matter Physics*. Cambridge Univ. Press, 2015.

[40] M Ammon and J. Erdmenger. *Gauge/Gravity Duality: Foundations and Applications*. Cambridge Univ. Press, 2015.

[41] T.J. Reber and et al. Power law liquid - a unified form of low-energy nodal electronic interactions in hole-doped cuprate superconductors. *Nat. Commun.*, 10:5737, 2019.

[42] C. Charmousis, B. Goutéraux, B. Soo Kim, E. Kiritsis, and R. Meyer. Effective holographic theories for low temperature. *J. High Energ. Phys.*, 2010:151, 2010.

[43] B. Goutéraux and E. Kiritsis. Generalized holographic quantum criticality at finite density. *J. High Energ. Phys.*, 2011:36, 2011.

[44] P. Kovtun. Lectures on hydrodynamic fluctuations in relativistic theories. *J. Phys. A: Math. Theor.*, 45:473001, 2001.

[45] A. Romero-Bermúdez, A. Krikun, K. Schalm, and J. Zaanen. Anomalous attenuation of plasmons in strange metals and holography. *Phys. Rev. B*, 99:235149, 2019.

[46] U. Gran, M. Tornsö, and T. Zingg. Holographic plasmons. *J. High Energ. Phys.*, 2018:176, 2018.

[47] E. H. Hwang and S. Das Sarma. Dielectric function, screening, and plasmons in two-dimensional graphene. *Phys. Rev. B*, 75:205418, May 2007.

[48] M. et al. Hepting. Three-dimensional collective charge excitations in electron-doped copper oxide superconductors. *Nature*, 563:374, 2018.

[49] A. Griffin and A. J. Pindor. Plasmon dispersion relations and the induced electron interaction in oxide superconductors: Numerical results. *Phys. Rev. B*, 39:11503, 1989.

[50] K. Schulte, D. Dulić, and G. A. Sawatzky. Plasmon dos in layered systems: two layers per unit cell. *Phys. C: Supercond.*, 317:554–557, 1999.

[51] A. et al. Legros. Universal t-linear resistivity and planckian dissipation in overdoped cuprates. *Nat. Phys.*, 15:142–147, 2019.

[52] Richard A Davison, Koenraad Schalm, and Jan Zaanen. Holographic duality and the resistivity of strange metals. *Physical Review B*, 89(24):245116, 2014.

[53] Patrick A Lee. Low-temperature t-linear resistivity due to umklapp scattering from a critical mode. *Physical Review B*, 104(3):035140, 2021.

[54] O. Takeo. High-resolution electron microscopy and electron diffraction of perovskite-type superconducting copper oxides. *Nanotechnol. Rev.*, 3:5, 2014.